Available online at www.sciencedirect.com
SCIENCE DIRECT®
Journal of Computational Physics 207 (2005) 736–768
JOURNAL OF COMPUTATIONAL PHYSICS
www.elsevier.com/locate/jcp

Improved boundary conditions for the direct numerical simulation of turbulent subsonic flows. I. Inviscid flows

R. Prosser *

Department of Mechanical, Aerospace and Civil Engineering, University of Manchester, P.O. Box 88, Manchester M60 1QD, UK

Received 16 June 2004; received in revised form 12 January 2005; accepted 27 January 2005
Available online 7 April 2005

Abstract

In the context of compressible flows, the standard non-reflecting boundary conditions of Hedstrom [J. Comput. Phys. 30 (1979) 222–237] produce spurious pressure oscillations when applied to turbulent flows. In this paper, we present an analysis of the characteristics used to define non-reflecting boundary conditions. The analysis is conducted in terms of a low Mach number asymptotic series. It is shown that the Hedstrom condition is not necessary for non-reflecting boundary conditions. Based on this analysis, new boundary conditions are presented. Crucially, the revised boundary conditions allow the specification of non-reflecting outflows and inflows. The new conditions are tested for three 2-dimensional inviscid flows: an inviscid vortex crossing an outflow boundary, an evolving vortex pair crossing an outflow, and a two dimensional turbulent flow with a prescribed energy spectrum. The new boundary conditions are found to perform considerably better than standard treatments in flows where vorticity crosses the boundary.

Keywords: Boundary conditions; Turbulence; Characteristics

1. Introduction

It is well known that the accuracy of a compressible flow calculation is strongly dependent on the choice of boundary conditions supplementing the governing equations. When the flow domain is closed, the boundary conditions imposed at walls and other geometrical features are comparatively straightforward to prescribe. If the flow domain is open, the boundary conditions' purpose is to provide a truncation of the physical problem to reduce the computational burden. Unfortunately, if the flow exiting the domain is turbulent, then the specification of the boundary conditions is challenging. The goal in this case is to

* Tel.: +44 161 200 3716; fax: +44 161 200 3723.
E-mail addresses: mcjssrp2@manchester.ac.uk, robert.prosser@manchester.ac.uk.

0021-9991/$ - see front matter
doi:10.1016/j.jcp.2005.01.027

Nomenclature

p	pressure
ρ	density
T	temperature
c_p	specific heat capacity
R	gas constant
x,y	inertial length scales (dimensionless)
ξ,θ	acoustic length scales (dimensionless)
t	time
s	entropy
u,v	velocity
M	flow Mach number
γ	adiabatic index
L_i	characteristic amplitude variation
ψ	stream function
u_b	mean flow speed
C	vortex strength
r_v	vortex radius
a	sound speed
$\widetilde{x}, \widetilde{y}$	dimensionless distances
l	domain size

Superscripts

(0), (1), ...	series index in low Mach number expansion
$'$	fluctuating quantity

Subscripts

0	reference quantities

prescribe boundary conditions that are as transparent to the numerical evolution of the flow as possible. Failure to do so can alter significantly the evolution of flow properties such as vorticity [2]. Turbulence comprises an (as yet) intractable spectrum of length and time scales, so obtaining a transparent boundary condition via the time dependency of the flow variables appears almost impossible in practice. The principal contribution of this paper is to attempt to provide a formalism that allows the specification of acoustically transparent inflow and outflow conditions for subsonic turbulent flows. The formalism we develop in this paper is a precursor to the treatment of viscous flows and, in particular, viscous flows with chemical reaction.

Considerable effort has been expended in the development of time dependent boundary conditions. In the review by Tsynkov [3], most artificial boundary conditions are classified according to two categories: global methods and local methods. In the former, the equations are expressed in an alternative setting, usually via one or more integral transforms [4,5]. The application of the boundary condition can then usually be expressed in terms of a pseudo-differential operator, the symbol of which is relatively simple in the transform domain, but non-local in the physical representation. The approach has the advantage of being accurate and robust. It is not, however, straightforward to implement in problems with complex geometries, nor

is it clear how one may generalize the approach to deal with the issues arising in the simulation of, say, viscous or reacting flows.

Local methods circumvent some of the implementation difficulties associated with global approaches. A family of local boundary conditions can be derived by approximating the symbol arising in a global method. The approximation is obtained by expressing the symbol as a Taylor series or as a Pade series, for example. Truncating the series leads to the desired approximate boundary conditions [4]. Due care has to exercised with the truncations, as not all of the resulting boundary conditions are stable [3,6]. This approach has the advantage of being easier to implement than a global method, but as it still requires the transformed equation system, it is again difficult to generalize to cases with additional physical complexity, such as turbulent flow systems.

A number of non-reflecting boundary conditions based on the method of characteristics have also been developed. These methods were originally designed for the linearized Euler system [1,7–10] but have been developed considerably. Among the more recent developments have been the Navier–Stokes characteristic boundary conditions (NSCBC) and the local one dimensional inviscid (LODI) approaches developed by Poinsot and Lele [11], Nicoud [12] and modified for reacting flows by Baum et al. [13,14], and by Sutherland and Kennedy [15].

Giles [6] provides a thorough development of time dependent boundary conditions for the linearized Euler equations. Central to this approach is the idea that the perturbations in the unsteady flow field are small when compared to the mean flow properties, as may be found in (for example) aeroacoustics applications. In this analysis, the LODI approach is seen to be a first order approximation to the null vectors associated with the dispersion relation derived from the linearized Euler system. The approach is known to be inadequate when the flow contains perturbations that are not driven purely by acoustics [5,6,16], and produces spurious pressure reflections. Grinstein [2] has observed that the application of one dimensional non-reflecting boundary conditions at an outflow can have significant effects on the vorticity distribution associated with free shear layers. The higher order asymptotic expansions developed by Giles to address this problem do not appear to provide significant improvements [6].

Colonius et al. [16] have attempted to extend the range of the characteristics based boundary conditions by treating the flow as a perturbation around a reference state that is in some sense 'near' to the actual flow evolution. They point out that such a reference flow need not satisfy the Navier–Stokes equations, but is rather an artifact designed to improve the accuracy of the linearization used to develop the boundary conditions. Even disregarding the difficulties of specifying an appropriate base flow in complex geometries, the results they presented were not significantly improved by this practise.

The aeroacoustics community is particularly sensitive to these issues, as the sound intensities associated with the flow turbulence can easily be swamped by both the discretization used and the boundary conditions imposed. In [16], Colonius et al. circumvented the problem of artificial noise by using characteristics based boundary conditions coupled to a *buffer zone*. In the buffer zone, the flow is damped by a combination of grid stretching and filtering. Turbulent fluctuations in the flow are damped to the point where the flow is approximately one dimensional and better represented by the linearized Euler equations. In their study, Colonius et al. found that the spurious reflections induced by the turbulence was reduced by 3 orders of magnitude by this approach. It has since been employed in a number of variants for aeroacoustics applications [17,18], for studies on turbulence itself [19] and even for reacting flow calculations [20,21].

Absorbing layers have also been used in approaches such as the perfectly matched layer (PML) technique. The PML equations are a superset of the Euler equations, with the incorporation of additional terms that act to reduce the size of the outgoing waves to zero, with little or no reflection at the boundary of the 'inner' domain. Like the characteristics based approaches, the PML method is based on the Euler system linearized about mean values for flow and fluid properties, and is particularly suited to aeroacoustics [22,23], although in its earlier forms it has been found to be ill-posed [24]. In common with other methods

based on the linearization of the Euler equation, it is unclear how the scheme could be extended to include viscous or other flow effects.

We have decided not to pursue the buffer layer approach in this paper. Partly this is due to the additional computational burden such approaches impose. The principal reason however is that there exist flow configurations (particularly when dealing with reacting flows) in which it is not clear where and when to apply the buffer layer. An example from reacting flow systems would be to simulate the experiments of Asato [25]. Such a study is of considerable importance to the combustion modelling community, and involves the simulation of a curved flame that crosses the computational boundary obliquely, attached to a stagnation plane. Where a buffer layer should be applied in this case, and its pervasive influence on the solution, is unclear. This paper therefore describes alternative boundary conditions that share many of the attractive features of the absorbing layer approach, but with the cheap computational costs of the characteristics based approach.

In the following paper, we develop alternative boundary conditions based on the characteristics of the inviscid components of the governing equations. The original component of the work stems from the application of a low Mach number expansion to provide an alternative specification of the incoming characteristics. We thereby demonstrate that it is possible to prescribe acoustically transparent inflow/outflow conditions for turbulence. The boundary conditions are tested on three problems

- A single vortex problem, where the vortex leaves the domain
- Two co-rotating vortices that evolve together and induce some reverse flow on the outflow boundary as they leave the domain.
- An inflow/outflow problem comprising a two dimensional, inviscid turbulent flow.

Section 2 highlights some of the problems with currently employed characteristics based approaches to boundary conditions, and Section 3 reviews the method of characteristics approach itself. In Section 4, low Mach number expansions of the governing equations and the associated characteristics are described. Through these expansions, the principal causes of the current difficulties are identified and discussed. Sections 5 and 6 provide modifications to the LODI method, to reduce the distorting effect of the boundary conditions. Results of the new approach are presented in Section 7. The paper ends with a discussion and some conclusions, both in Section 8.

2. Current non-reflecting boundary conditions in turbulent flows

Fig. 1 shows the time evolution of the vorticity field induced by a single, two dimensional inviscid vortex. The initial conditions for this flow field were calculated using a stream function and velocity field defined by

$$\begin{aligned} \psi &= C\exp\left(-\frac{r^2}{2r_v^2}\right) + u_b y, \\ u &= \frac{\partial \psi}{\partial y}, \\ v &= -\frac{\partial \psi}{\partial x}, \end{aligned} \tag{1}$$

where $r = \sqrt{x^2 + y^2}$, C is the vortex strength, u_b is the mean velocity and r_v is a characteristic radius. For this simulation, C was set at 5×10^{-3} m^2/s, r_v was set at 10% of the domain size and the mean velocity u_b was set at 2 m/s. The pressure, density and temperature were obtained from an analytic solution (given in Section 7). The simulation was carried out using spanwise periodic boundary conditions, with a reflecting inflow condition and a standard LODI non-reflecting outflow condition.

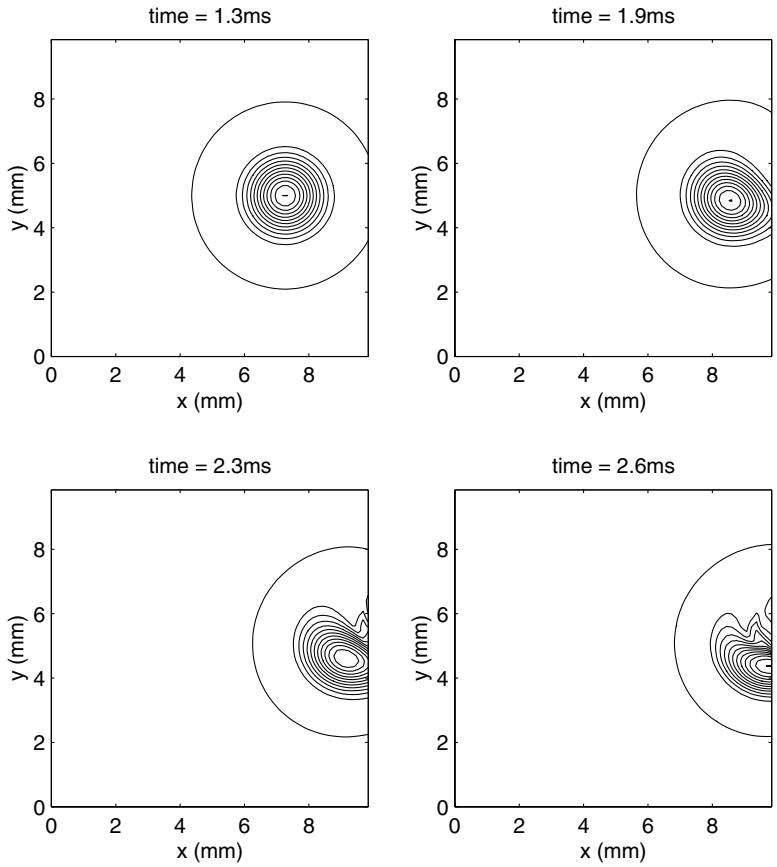

Fig. 1. Distortion of a 2D vortex as it crosses a non-reflecting outflow.

For inviscid, two dimensional flows at low Mach numbers, vorticity is essentially a conserved scalar [26]. Consequently, we expect that the isovorticity contours of the case represented in Fig. 1 to be convected out of the domain without deformation. We see from the vorticity contour plots that significant deformation of the flow structure has occurred as the vortex crosses the boundary. Furthermore, for a low-speed flow, we expect the dynamic pressure to be related to the velocity field by

$$\Delta p \sim \frac{1}{2}\rho\left((u')^2 + (v')^2\right), \tag{2}$$

where u' and v' are the velocity perturbations measured relative to the mean velocity (an exact relationship will be established in Section 7). Fig. 2 shows the pressure field corresponding to a simulation time of 2.6 ms. The dynamic pressure distribution in the figure is distorted and is larger than the estimate provided by Eq. (2) by approximately 2 orders of magnitude.

If the single vortex is replaced with two dimensional inviscid turbulent flow, it becomes more difficult to identify boundary induced distortions in the flow vorticity, although significant perturbations in the pressure field can still be seen. Fig. 3 shows the evolution of the pressure field associated with a turbulent flow moving with a mean velocity of 2 m/s; the initial conditions for this flow are derived via a prescribed energy spectrum, and are described in Section 7. The initial conditions for the simulation have a dynamic pressure field that satisfies the estimate in Eq. (2). Fig. 3 shows the initial pressure field and its subsequent evolution

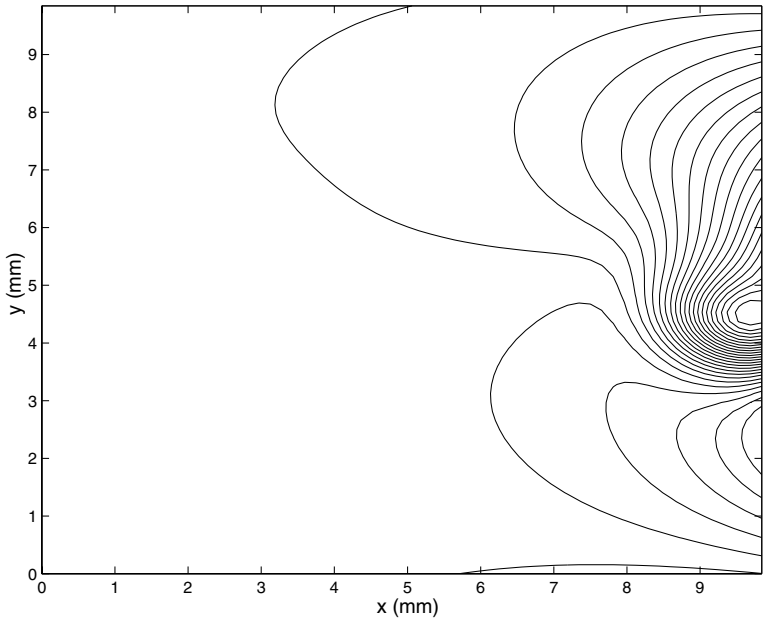

Fig. 2. Distortion of pressure field as vortex crosses standard non-reflecting boundary. Pressure isocontours should be concentric circles.

for a short period after the simulation begins. Violent pressure fluctuations originate at the outlet boundary and propagate upstream at the local sound speed. By the end of an acoustic transit time (defined as the time required for an acoustic wave to cross the domain $\sim l_0\sqrt{\rho_0/\gamma p_0}$), the pressure field contains perturbations up to two orders of magnitude greater than that approximated by Eq. (2). In the following sections, we provide a description of the source of this error, and propose revisions to the non-reflecting boundary conditions to rectify it.

3. Governing equations

For the two dimensional problems considered in this paper, the compressible Euler equations can be written in dimensionless form as

$$\frac{\partial \rho}{\partial t} + u\frac{\partial \rho}{\partial \widetilde{x}} + v\frac{\partial \rho}{\partial \widetilde{y}} + \rho\left(\frac{\partial u}{\partial \widetilde{x}} + \frac{\partial v}{\partial \widetilde{y}}\right) = 0, \tag{3a}$$

$$\frac{\partial u}{\partial t} + u\frac{\partial u}{\partial \widetilde{x}} + v\frac{\partial u}{\partial \widetilde{y}} + \frac{1}{\rho M^2}\left(\frac{\partial p}{\partial \widetilde{x}}\right) = 0, \tag{3b}$$

$$\frac{\partial v}{\partial t} + u\frac{\partial v}{\partial \widetilde{x}} + v\frac{\partial v}{\partial \widetilde{y}} + \frac{1}{\rho M^2}\left(\frac{\partial p}{\partial \widetilde{y}}\right) = 0, \tag{3c}$$

$$\frac{\partial p}{\partial t} + u\frac{\partial p}{\partial \widetilde{x}} + v\frac{\partial p}{\partial \widetilde{y}} + \gamma p\left(\frac{\partial u}{\partial \widetilde{x}} + \frac{\partial v}{\partial \widetilde{y}}\right) = 0. \tag{3d}$$

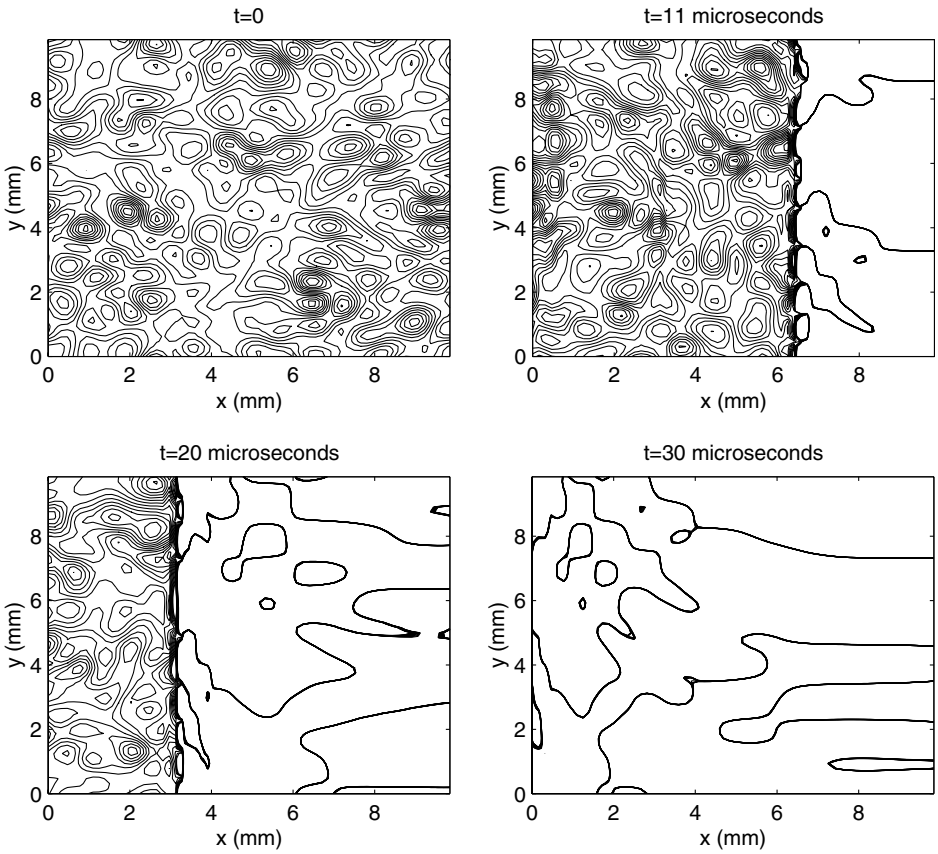

Fig. 3. Evolution of spurious pressure disturbance for a turbulent flow with standard non-reflecting outflow boundary conditions. The left moving wave contains pressure perturbations that are two orders of magnitude larger than those estimated by Eq. (2).

In Eqs. (3a)–(3d), the variables have been non-dimensionalized with respect to a length scale characterizing the domain size l_0, a density ρ_0 and a velocity u_0, which is assumed to be small with respect to the local sound speed. Under these assumptions, the Mach number appearing in Eqs. (3b) and (3c) is small. Thermodynamic quantities such as c_p, c_v, and R, which appear later in the paper, are assumed to be constant throughout; $(c_p)_0 \equiv c_p$ is used to non-dimensionalize these quantities. The pressure has been non-dimensionalized with respect to a thermodynamic pressure $\gamma\rho_0 RT_0$, where T_0 is an absolute temperature and γ is introduced to simplify the algebra later in the analysis. Using these variables, the local sound speed in dimensionless coordinates is $a = M^{-1}(\gamma p/\rho)^{\frac{1}{2}}$.

We follow the procedure described by Thompson [7] and by Poinsot and Lele [11], and re-write the Euler system in terms of characteristic variables. A one-dimensional approximation is invoked, where the transverse terms at the boundary are temporarily omitted from the analysis. The characteristic terms are derived, and are then substituted back into the original multidimensional equations. Further details of the method are sketched in Appendix B, and a full account can be found in [11].

For definiteness, we consider a two dimensional domain whose boundaries are aligned with the $\tilde{x}$ and $\tilde{y}$ axes. For the purposes of this paper, the left hand boundary will be located at $\tilde{x} = 0$ and will be assumed to be the inlet. The right hand boundary will be located at $\tilde{x} = 1$, and will be taken to be the outlet. Spanwise

periodicity will be assumed for the top and bottom boundaries. Along the inlet and outlet boundaries, Eqs. (3a)–(3d) are replaced with

$$\frac{\partial \rho}{\partial t} + \frac{\rho}{T}(L_1 + L_4) - \frac{\rho}{c_p} L_2 + v\frac{\partial \rho}{\partial \widetilde{y}} + \rho \frac{\partial v}{\partial \widetilde{y}} = 0, \tag{4a}$$

$$\frac{\partial u}{\partial t} + \frac{1}{MT}\sqrt{\frac{\gamma p}{\rho}}(L_4 - L_1) + v\frac{\partial u}{\partial \widetilde{y}} = 0, \tag{4b}$$

$$\frac{\partial v}{\partial t} + L_3 + v\frac{\partial v}{\partial \widetilde{y}} + \frac{1}{\rho M^2}\frac{\partial p}{\partial \widetilde{y}} = 0, \tag{4c}$$

$$\frac{\partial p}{\partial t} + \rho c_p (L_4 + L_1) + \gamma p \frac{\partial v}{\partial \widetilde{y}} + v\frac{\partial p}{\partial \widetilde{y}} = 0. \tag{4d}$$

In these equations, the dimensionless specific heats $c_p(\equiv 1)$ and $c_v(\equiv \gamma^{-1})$ are kept explicitly to help clarify the algebra when the equations are re-expressed in their dimensional form. The variables L_1 to L_4 are the *characteristic variable amplitude variations* (or *amplitudes* for short) and are defined as

$$\begin{aligned}
L_1 &= \frac{1}{2\rho c_p}\left(u - \frac{1}{M}\sqrt{\frac{\gamma p}{\rho}}\right)\left(\frac{\partial p}{\partial \widetilde{x}} - M\sqrt{\gamma \rho p}\frac{\partial u}{\partial \widetilde{x}}\right),\\
L_2 &= u\left(c_v\left(\frac{1}{p}\frac{\partial p}{\partial \widetilde{x}} - \frac{\gamma}{\rho}\frac{\partial \rho}{\partial \widetilde{x}}\right)\right) = u\frac{\partial s}{\partial \widetilde{x}},\\
L_3 &= u\frac{\partial v}{\partial \widetilde{x}},\\
L_4 &= \frac{1}{2\rho c_p}\left(u + \frac{1}{M}\sqrt{\frac{\gamma p}{\rho}}\right)\left(\frac{\partial p}{\partial \widetilde{x}} + M\sqrt{\gamma \rho p}\frac{\partial u}{\partial \widetilde{x}}\right).
\end{aligned} \tag{5}$$

We adopt a nomenclature akin to that of Yee et al. [27], and refer to L_1 and L_4 specifically as non-linear amplitudes. At the inlet boundary, conditions must be specified for the unknown incoming amplitudes L_2, L_3 and L_4. For the outlet boundary, the only incoming amplitude requiring specification is L_1. The standard non-reflecting boundary conditions [1,7] are obtained by setting all incoming amplitudes to zero. A range of other practical boundary conditions can be specified by appropriate matching of incoming or outgoing amplitudes [11,13].

4. Low Mach number expansions

In the following section, we outline some preliminary results and observations that will be later exploited to provide acoustically transparent boundary conditions. These boundary conditions do not suffer from the large pressure field oscillations of the current treatments.

Guidance for the boundary conditions in the case of low flow Mach numbers is provided by a two step process. The first step is to express all of the dependent variables in terms of a low Mach number expansion [28], i.e., the pressure is written as $p = p^{(0)} + Mp^{(1)} + M^2 p^{(2)} + \mathrm{O}(M^3)$. Bracketed, superscripted numbers are used to index the terms in a given expansion. The second step is to introduce two separate length scales: an inertial length scale l_i and an acoustic length scale l_a. This decomposition is due to Klein [29], and the references cited therein. We repeat the justification for it here for completeness. Consider a compressible turbulent flow, and let t_ref be a timescale associated with that flow (an example might be a LETOT, or large Eddy turn over time). The turbulence has associated with it a characteristic velocity u, and consequently an

inertial length scale can be written as $l_i = ut_{ref}$. Simultaneously with the turbulence, acoustic waves propagate through the domain with a characteristic velocity a, and so an acoustic length scale can be defined as $l_a = at_{ref}$. Using the LETOT example, l_i is an inertial length scale associated with a large eddy in the flow, and l_a is the distance covered by an acoustic wave in one LETOT.

It is readily seen that $l_i/l_a = M$, a characteristic Mach number. Consequently, it appears appropriate to introduce two spatial length scales into the low Mach number expansions: $\mathbf{x} = (x,y)^T$ and $M\mathbf{x} = \boldsymbol{\eta} = (\xi,\theta)^T$. Using this decomposition, the derivatives appearing in the Euler equations are expressed as (in the case of the $\widetilde{x}$ derivative)

$$\left.\frac{\partial}{\partial \widetilde{x}}\right|_{M,t} = \frac{\partial}{\partial x} + M\frac{\partial}{\partial \xi}.$$

The full decomposition for momentum, continuity and the energy variables are presented in Appendix A. From the momentum equation, we find that $p^{(0)} = \text{const}$, $p^{(1)} = p^{(1)}(\xi,\theta)$ and

$$\frac{\partial u^{(0)}}{\partial t} + u^{(0)}\frac{\partial u^{(0)}}{\partial x} + v^{(0)}\frac{\partial u^{(0)}}{\partial y} + \frac{1}{\rho^{(0)}}\left(\frac{\partial p^{(2)}}{\partial x} + \frac{\partial p^{(1)}}{\partial \xi}\right) = 0,$$

$$\frac{\partial v^{(0)}}{\partial t} + u^{(0)}\frac{\partial v^{(0)}}{\partial x} + v^{(0)}\frac{\partial v^{(0)}}{\partial y} + \frac{1}{\rho^{(0)}}\left(\frac{\partial p^{(2)}}{\partial y} + \frac{\partial p^{(1)}}{\partial \theta}\right) = 0.$$

The equation for the *acoustic* pressure is

$$\frac{\partial p^{(1)}}{\partial t} + \gamma p^{(0)}\left(\frac{\partial u^{(0)}}{\partial \xi} + \frac{\partial v^{(0)}}{\partial \theta}\right) = 0 \tag{6}$$

and it is shown in Appendix A that the leading order velocity field is divergence free over the inertial length scales;

$$\frac{\partial u^{(0)}}{\partial x} + \frac{\partial v^{(0)}}{\partial y} = 0.$$

If the same methodology is applied to the non-linear amplitudes, we find

$$\begin{aligned} L_1 &= L_1^{(0)} + ML_1^{(1)} + \cdots \\ &= \frac{1}{2\rho^{(0)}c_p}\left(\gamma p^{(0)}\frac{\partial u^{(0)}}{\partial x} + M\left(\gamma p^{(0)}\left(\frac{\partial u^{(0)}}{\partial \xi} + \frac{\partial u^{(1)}}{\partial x} + \frac{\partial u^{(0)}}{\partial x}\left(\frac{p^{(1)}}{p^{(0)}} - \frac{\rho^{(1)}}{\rho^{(0)}}\right)\right)\right.\right. \\ &\quad \left.\left. - \sqrt{\frac{\gamma p^{(0)}}{\rho^{(0)}}}\left\{\frac{\partial p^{(1)}}{\partial \xi} + \frac{\partial p^{(2)}}{\partial x} + \rho^{(0)}u^{(0)}\frac{\partial u^{(0)}}{\partial x}\right\}\right)\right) + \mathrm{O}(M^2), \end{aligned} \tag{7}$$

$$\begin{aligned} L_4 &= L_4^{(0)} + ML_4^{(1)} + \cdots \\ &= \frac{1}{2\rho^{(0)}c_p}\left(\gamma p^{(0)}\frac{\partial u^{(0)}}{\partial x} + M\left(\gamma p^{(0)}\left(\frac{\partial u^{(0)}}{\partial \xi} + \frac{\partial u^{(1)}}{\partial x} + \frac{\partial u^{(0)}}{\partial x}\left(\frac{p^{(1)}}{p^{(0)}} - \frac{\rho^{(1)}}{\rho^{(0)}}\right)\right)\right.\right. \\ &\quad \left.\left. + \sqrt{\frac{\gamma p^{(0)}}{\rho^{(0)}}}\left\{\frac{\partial p^{(1)}}{\partial \xi} + \frac{\partial p^{(2)}}{\partial x} + \rho^{(0)}u^{(0)}\frac{\partial u^{(0)}}{\partial x}\right\}\right)\right) + \mathrm{O}(M^2). \end{aligned} \tag{8}$$

Expressions for L_2 and L_3 can also be derived (see Appendix A), but these will not play an immediate role in the subsequent analyses.

5. Non-reflecting convective outflows

5.1. The source of the flow distortions

Using the definitions given earlier for the computational domain, the standard non-reflecting outflow boundary condition is obtained by setting $L_1 = 0$, possibly with $L_2 = 0$ and $L_3 = 0$, depending on the local flow structure. The dominant effects induced by these specifications arise from the condition imposed on L_1. Examining the leading order and O(M) terms of Eq. (7), we see that $L_1 = 0$ imposes the following conditions on the incoming amplitude:

$$L_1^{(0)} = 0 \Rightarrow \frac{\partial u^{(0)}}{\partial x} = 0, \tag{9}$$

$$L_1^{(1)} = 0 \Rightarrow \gamma p^{(0)} \left(\frac{\partial u^{(0)}}{\partial \xi} + \frac{\partial u^{(1)}}{\partial x} \right) = \sqrt{\frac{\gamma p^{(0)}}{\rho^{(0)}}} \left\{ \frac{\partial p^{(1)}}{\partial \xi} + \frac{\partial p^{(2)}}{\partial x} \right\}. \tag{10}$$

We now consider the effect of the non-reflecting condition on, say, the evolution of the pressure (Eq. (4d)). The leading order pressure transport equation is

$$\frac{\partial p^{(0)}}{\partial t} = -\rho^{(0)} c_p \left(L_4^{(0)} + L_1^{(0)} \right) - \gamma p^{(0)} \frac{\partial v^{(0)}}{\partial y}. \tag{11}$$

$L_4^{(0)}$ is retained in this equation, as it is the leading order component of an outgoing amplitude and is calculated as part of the solution. However, the incorporation of Eq. (9) via the non-reflecting condition modifies Eq. (11) to

$$\frac{\partial p^{(0)}}{\partial t} = -\gamma p^{(0)} \left(\frac{1}{2} \frac{\partial u^{(0)}}{\partial x} + \frac{\partial v^{(0)}}{\partial y} \right) = \gamma p^{(0)} \frac{1}{2} \frac{\partial u^{(0)}}{\partial x} \tag{12}$$

on the boundary. For the low Mach number flow problems considered in this paper, the thermodynamic pressure remains constant in time and space. This then implies that the leading order pressure term should satisfy $\partial p^{(0)}/\partial t = 0$. Eq. (12) (which, we recall, emerges from the application of the boundary condition) only guarantees the correct behaviour for the thermodynamic pressure if

$$\partial u^{(0)}/\partial x = 0$$

on the boundary, i.e., if there is no turbulence, straining or other dynamic fluid behaviour. In the general case there are velocity gradients on the boundary, and consequently the calculated values for $\partial p^{(0)}/\partial t$ are non-zero. We conclude that the significant pressure fluctuations observed in Fig. 3 are manifestations of the boundary conditions' inability to enforce the leading order continuity equation. A similar equation can be written for $u^{(0)}$. This also contains significant distortions arising from the non-reflecting condition.

5.2. An alternative non-reflecting criterion

For a simulation without turbulence, mean shear, etc., the equation for the incoming amplitude on an outflow is derived from Eq. (7) by removing all inertial length scale terms. Such a simplified flow configuration may be obtained by, say, putting the computational boundaries far from any turbulence:

$$L_1 = \frac{1}{2\rho^{(0)} c_p} M \left(\gamma p^{(0)} \frac{\partial u^{(0)}}{\partial \xi} - \sqrt{\frac{\gamma p^{(0)}}{\rho^{(0)}}} \frac{\partial p^{(1)}}{\partial \xi} \right) + \mathrm{O}(M^2). \tag{13}$$

The standard non-reflecting boundary condition $L_1 = 0$ on such an outflow provides

$$\sqrt{\rho^{(0)}\gamma p^{(0)}}\frac{\partial u^{(0)}}{\partial \xi} - \frac{\partial p^{(1)}}{\partial \xi} = 0. \tag{14}$$

We arrive at our central observation: *the standard non-reflecting condition should be applied to the acoustic length scale features of the flow only*. The similarity between Eq. (14) and the more widely used non-reflecting condition

$$L_1 = 0 \Rightarrow \sqrt{\rho\gamma p}\frac{\partial u}{\partial \tilde{x}} - \frac{\partial p}{\partial \tilde{x}} = 0 \tag{15}$$

is apparent. The traditional non-reflecting condition, imposed via Eq. (15) also satisfies Eq. (14), but in the process distorts the flow by the imposition of Eqs. (9) and (10). Eq. (15) is sufficient but not necessary for non-reflecting behaviour.

Reverting to flows which do have inertial scale structure, and incorporating the revised non-reflecting condition (Eq. (14)) into Eq. (7), the incoming amplitude becomes

$$L_1 = \frac{1}{2\rho^{(0)}c_p}\left(\gamma p^{(0)}\frac{\partial u^{(0)}}{\partial x} + M\left(\gamma p^{(0)}\left(\frac{\partial u^{(1)}}{\partial x} + \frac{\partial u^{(0)}}{\partial x}\left(\frac{p^{(1)}}{p^{(0)}} - \frac{\rho^{(1)}}{\rho^{(0)}}\right)\right) - \sqrt{\frac{\gamma p^{(0)}}{\rho^{(0)}}}\left\{\frac{\partial p^{(2)}}{\partial x} + \rho^{(0)}u^{(0)}\frac{\partial u^{(0)}}{\partial x}\right\}\right)\right) + \mathrm{O}(M^2).$$

L_1 contains essentially the same inertial scale elements as L_4, *but has had all acoustic behaviour removed*. The treatments for L_2 and L_3 will be discussed in the following sections.

5.3. Incorporating convective and acoustic effects

Matching the leading and first orders of the u-momentum equation (Eq. (4b)) provides the following relationships for the leading orders of the incoming non-linear amplitude L_1;

$$L_1^{(0)} = L_4^{(0)}, \tag{16}$$

$$\frac{\partial u^{(0)}}{\partial t} + \frac{1}{T^{(0)}}\sqrt{\frac{\gamma p^{(0)}}{\rho^{(0)}}}\left(L_4^{(1)} - L_1^{(1)}\right) + v^{(0)}\frac{\partial u^{(0)}}{\partial y} = 0. \tag{17}$$

$L_1^{(0)}$ and $L_4^{(0)}$ contain the inertial terms required to ensure that the continuity equation, and hence the thermodynamic pressure, is properly maintained. A convective boundary condition can be applied to the inertial components of the flow by using the frozen turbulence hypothesis;

$$\frac{\partial u^{(0)}}{\partial t} = -u_b\frac{\partial u^{(0)}}{\partial x},$$

where u_b is the mean velocity. In many applications, the mean flow speed emerges as part of the solution procedure and is difficult to specify a priori. We have tried replacing u_b with the local instantaneous u velocity to see what influence such a modification would have on the solution. When we tried this approach, we found that the resulting pressure distributions were slightly less accurate than those we present here, although the long term stability of the algorithm did not appear to have been significantly altered.

Substituting this approximation into Eq. (17), we obtain

$$L_1^{(1)} = L_4^{(1)} + T^{(0)}\sqrt{\frac{\rho^{(0)}}{\gamma p^{(0)}}}\left(v^{(0)}\frac{\partial u^{(0)}}{\partial y} - u_b\frac{\partial u^{(0)}}{\partial x}\right). \tag{18}$$

Eq. (18) provides a *reflecting* outflow boundary condition. The reason for this is revealed via an examination of $L_4^{(1)}$ (Eq. (8)), which can be seen to contain a right-going acoustic term of the form

$$\frac{1}{2\rho^{(0)}c_p}\left(\gamma p^{(0)}\frac{\partial u^{(0)}}{\partial \xi}+\sqrt{\frac{\gamma p^{(0)}}{\rho^{(0)}}}\frac{\partial p^{(1)}}{\partial \xi}\right).$$

From the discussion in the previous section, $L_1^{(1)}$ must contain no acoustic components at all. To remove the reflecting behaviour, we therefore modify Eq. (18) in a two step process. Firstly, the acoustic behaviour carried implicitly by $L_4^{(1)}$ is explicitly removed;

$$L_1^{(1)}=L_4^{(1)}+T^{(0)}\sqrt{\frac{\rho^{(0)}}{\gamma p^{(0)}}}\left(v^{(0)}\frac{\partial u^{(0)}}{\partial y}-u_b\frac{\partial u^{(0)}}{\partial x}\right)-\frac{1}{2\rho^{(0)}c_p}\left(\gamma p^{(0)}\frac{\partial u^{(0)}}{\partial \xi}+\sqrt{\frac{\gamma p^{(0)}}{\rho^{(0)}}}\frac{\partial p^{(1)}}{\partial \xi}\right). \tag{19}$$

Secondly, the revised non-reflecting (Eq. (14)) is substituted into Eq. (19), to obtain

$$L_1^{(1)}=L_4^{(1)}+T^{(0)}\sqrt{\frac{\rho^{(0)}}{\gamma p^{(0)}}}\left(v^{(0)}\frac{\partial u^{(0)}}{\partial y}-u_b\frac{\partial u^{(0)}}{\partial x}\right)-\frac{\gamma p^{(0)}}{\rho^{(0)}c_p}\frac{\partial u^{(0)}}{\partial \xi}. \tag{20}$$

The resulting formulation exhibits the correct wave behaviour for the acoustics on the boundary. To demonstrate this last point, we note that if Eq. (20) is substituted into Eq. (17), we obtain the resultant time dependent behaviour of $u^{(0)}$ on the boundary,

$$\frac{\partial u^{(0)}}{\partial t}+u_b\frac{\partial u^{(0)}}{\partial x}+\sqrt{\frac{\gamma p^{(0)}}{\rho^{(0)}}}\frac{\partial u^{(0)}}{\partial \xi}=0, \tag{21}$$

$u^{(0)}$ is thus seen to have both the convective outflow component and an outgoing acoustic wave-like behaviour.

To calculate the acoustic term $\partial(u^{(0)})/\partial\xi$, we recall that, to leading order

$$\frac{1}{M}\sqrt{\frac{\overline{\gamma p}}{\rho}}\left(\frac{\partial u}{\partial \widetilde{x}}+\frac{\partial v}{\partial \widetilde{y}}\right)=\sqrt{\frac{\gamma p^{(0)}}{\rho^{(0)}}}\left(\frac{\partial u^{(0)}}{\partial \xi}+\frac{\partial v^{(0)}}{\partial \theta}\right)\simeq\sqrt{\frac{\gamma p^{(0)}}{\rho^{(0)}}}\frac{\partial u^{(0)}}{\partial \xi}. \tag{22}$$

Eq. (22) is obtained by assuming that all acoustic activity in the domain produces planar waves that approach the boundary at normal incidence. This restraint is consistent with the widely used LODI and NSCBC approaches [11,13] and implies $\partial(v^{(0)})/\partial\theta=0$.

5.4. Behaviour of the boundary conditions as $M\to 1$

Eq. (21) appears to give the correct acoustic wave speed only for flows with a low mean velocity. As the mean flow speed increases, we would expect an additional $u_b(\partial u^{(0)}/\partial\xi)$ term to appear in the Eq. (21). This additional term would ensure that the resultant acoustic wave equation exhibits the correct dependence on the *local* sound speed. As this dependence is not apparent in Eq. (21), it appears that the boundary conditions must fail as the Mach number becomes significant. We will now demonstrate that this is *not* the case.

We consider again the amplitudes L_1 and L_5. To simplify the algebra, we will assume that there are no inertial effects in the flow under consideration, and examine the reflective properties of the boundary conditions as $M\to 1$. Under these assumptions, Eqs. (7) and (8) can be written as

$$2\rho c_p L_1 = -M\sqrt{\frac{\gamma p^{(0)}}{\rho^{(0)}}}\left(\frac{\partial p^{(1)}}{\partial \xi} - \sqrt{(\gamma p_0 \rho_0)}\frac{\partial u^{(0)}}{\partial \xi}\right) + M^2\left(\left(u^{(0)} + u_b\right)\left(\frac{\partial p^{(1)}}{\partial \xi} - \sqrt{(\gamma p_0 \rho_0)}\frac{\partial u^{(0)}}{\partial \xi}\right) + R_1\right) + \mathrm{O}(M^3), \tag{23}$$

$$2\rho c_p L_5 = M\sqrt{\left(\gamma\frac{p_0}{\rho_0}\right)}\left(\frac{\partial p^{(1)}}{\partial \xi} + \sqrt{(\gamma p_0 \rho_0)}\frac{\partial u^{(0)}}{\partial \xi}\right) + M^2\left(\left(u^{(0)} + u_b\right)\left(\frac{\partial p^{(1)}}{\partial \xi} + \sqrt{(\gamma p_0 \rho_0)}\frac{\partial u^{(0)}}{\partial \xi}\right) + R_2\right) + \mathrm{O}(M^3). \tag{24}$$

In these equations, the terms R_1 and R_2 are residuals arising from the expansion of the amplitudes. Unlike the first term of the $\mathrm{O}(M^2)$ components in Eqs. (23) and (24), both R_1 and R_2 remain $\mathrm{O}(M^2)$ irrespective of the flow speed and consequently do not affect the acoustic wave equations. Suppose now that the sum of the bulk velocity and the leading order velocity perturbation approaches the speed of sound. In dimensionless coordinates, this implies that

$$u^{(0)} + u_b \to \frac{1}{M}\sqrt{\frac{\gamma p^{(0)}}{\rho^{(0)}}}.$$

Consequently, the first term in the $\mathrm{O}(M^2)$ components of Eqs. (23) and (24) becomes $\mathrm{O}(M)$ and hence we obtain

$$2\rho c_p L_1 = -M\left(\left(u^{(0)} + u_b\right) - \sqrt{\left(\gamma\frac{p_0}{\rho_0}\right)}\right)\left(\frac{\partial p^{(1)}}{\partial \xi} - \sqrt{(\gamma p_0 \rho_0)}\frac{\partial u^{(0)}}{\partial \xi}\right) + \mathrm{O}(M^2),$$

$$2\rho c_p L_5 = M\left(\left(u^{(0)} + u_b\right) + \sqrt{\left(\gamma\frac{p_0}{\rho_0}\right)}\right)\left(\frac{\partial p^{(1)}}{\partial \xi} + \sqrt{(\gamma p_0 \rho_0)}\frac{\partial u^{(0)}}{\partial \xi}\right) + \mathrm{O}(M^2)$$

as $M \to 1$. Performing a similar analysis as that which led to Eq. (21), and using the modified definitions of L_1 and L_4, we observe that for high speed flows

$$\frac{\partial u^{(0)}}{\partial t} + \left(\left(u_b + u^{(0)}\right) + \sqrt{\frac{\gamma p^{(0)}}{\rho^{(0)}}}\right)\frac{\partial u^{(0)}}{\partial \xi} = 0. \tag{25}$$

We conclude that the wave equation derived using the approach given in the previous sections does indeed produce the correct acoustic wave propagation behaviour as the mean flow speed increases to $M = 1$. At some cost in algebra, Eq. (25) can be rederived with inertial effects taken into account.

We note finally that for outflow boundaries, the eigenvalue associated with the incoming amplitude tends to zero as the local mean flow speed approaches the speed of sound. Consequently, the contribution from the incoming wave amplitude decreases relative to the outgoing wave. It follows that the maximum error due to the boundary conditions should be incurred at low flow speeds, where the incoming and outgoing amplitudes are essentially in balance. Results demonstrating the performance of the boundary conditions for a turbulent flow with a mean flow Mach number of 1.5 will be given below.

5.5. Final boundary conditions for non-reflecting behaviour

Re-casting Eq. (20) into a fully dimensional form, and with a slight abuse of notation, the new non-reflecting outflow condition for L_1 can be written in one of two forms;

$$L_1 = L_4 + \frac{(\gamma-1)T}{a}\left(v\frac{\partial u}{\partial y} - (u_b + a)\frac{\partial u}{\partial x} - a\frac{\partial v}{\partial y}\right), \tag{26a}$$

$$L_1 = L_4 + \frac{(\gamma-1)T}{a}\left(v\frac{\partial u}{\partial y} + (u_b - a)\frac{\partial v}{\partial y} - a\frac{\partial u}{\partial x}\right), \tag{26b}$$

where

$$a\left(\frac{\partial u}{\partial x} + \frac{\partial v}{\partial y}\right) \simeq \sqrt{\frac{\gamma p^{(0)}}{\rho^{(0)}}}\frac{\partial u^{(0)}}{\partial \xi} \tag{27}$$

has been incorporated.

For the remaining amplitudes L_2 and L_3, we assume that the Hedstrom conditions hold [1];

$$L_2 = \begin{cases} u\frac{\partial s}{\partial x} & \text{wave is outgoing,} \\ 0 & \text{wave is incoming,} \end{cases}$$

$$L_3 = \begin{cases} u\frac{\partial v}{\partial x} & \text{wave is outgoing,} \\ 0 & \text{wave is incoming.} \end{cases} \tag{28}$$

It is possible to show that the ratio of L_3 to L_1 is O(M), and that of L_2 to L_1 is O(M^2). Consequently, an error in prescribing L_2 and L_3 via Eq. (28) is only going to have a small effect. Errors in the prescription of L_2 and L_3 arise in turbulent flows where a flow recirculation momentarily attempts to drive the fluid back into the domain across the outflow. In this case, the exact flow structure that should be driven back into the domain via the recirculation is unknown, and the amplitude variations must be set to zero. As both L_2 and L_3 move with the local fluid velocity, any errors associated with them are convected at the same speed. It follows that, provided the rms intensity of the turbulence is less than the mean flow speed, the errors will be convected out of the domain.

6. Non-reflecting turbulent inflows

6.1. The standard practice

In the standard LODI approach, inlet conditions are prescribed via an appropriate balancing of the characteristic amplitudes. As an example, a steady inlet condition for u-velocity, using the LODI approximation, would be obtained from Eq. (4b) by specifying $L_4 = L_1$. By definition, this approach presupposes no transverse variations in the flow field along the inlet. For a turbulent inflow, all of the time derivatives of the dependent variables are non-zero and the flow has significant transverse structure, thereby precluding such simple specification.

Current practice for generating turbulent inlet boundary conditions is as follows. First, a preliminary calculation is undertaken to generate a turbulent flow field with zero mean velocity. This turbulent flow field is often calculated using periodic boundary conditions, so that highly accurate spectral methods can be used to produce the initial conditions. Once the turbulent field has evolved to the required statistical state, a snapshot is taken. The snapshot is an instantaneous realization of the flow field, which we will refer to as the *frozen solution*.

A Galilean transformation is applied to the frozen solution, matching its mean velocity with that of the main simulation. The flux functions from the transformed frozen solution are used to specify $\frac{\partial}{\partial t}(\mathbf{U})_{\text{in}}$. The LODI approach then balances the incoming amplitudes against the computed outgoing amplitudes, such

that $\frac{\partial}{\partial t}(\mathbf{U})_{\text{in}}$ is exactly enforced on the boundary. As $\frac{\partial}{\partial t}(\mathbf{U})_{\text{in}}$ is rigidly fixed at the inlet by this method, the resulting boundary condition is fully reflecting.

The reflection is caused by equating (say) L_1 and L_4 to obtain the exact values for $\frac{\partial}{\partial t}(u)_{\text{in}}$ and $\frac{\partial}{\partial t}(p)_{\text{in}}$. We have shown that L_1 and L_4 essentially share 'inertial length scale' elements, but not acoustic phenomena. Matching L_1 and L_4 without taking into account the different acoustic behaviour of the amplitudes leads to the observed reflection.

6.2. The revised procedure

To eliminate the reflective behaviour, we adopt the following procedure. The same methodology using the frozen solution is adopted. Rather than obtaining $\frac{\partial}{\partial t}(\mathbf{U})_{\text{in}}$ via a Galilean transformation of the flux functions however, we derive $\frac{\partial}{\partial t}(\mathbf{U})_{\text{in}}$ via a Galilean transformation of the *incoming amplitudes*. For the inflow conditions required here, we read the incoming amplitudes directly from the frozen solution. The incoming amplitudes will, by construction, have the following low Mach number expansions.

$$L_2 = \left(u^{(0)} + u_b\right)c_v\left(\frac{1}{p^{(0)}}\frac{\partial p^{(2)}}{\partial x} - \frac{\gamma}{\rho^{(0)}}\frac{\partial \rho^{(2)}}{\partial x}\right)M^2 + \mathrm{O}(M^3), \tag{29}$$

$$L_3 = \left(u^{(0)} + u_b\right)\frac{\partial v^{(0)}}{\partial x} + \mathrm{O}(M), \tag{30}$$

$$L_4 = \frac{1}{2\rho^{(0)}c_p}\left(\gamma p^{(0)}\frac{\partial u^{(0)}}{\partial x} + M\left(\gamma p^{(0)}\frac{\partial u^{(0)}}{\partial x}\left(\frac{p^{(1)}}{p^{(0)}} - \frac{\rho^{(1)}}{\rho^{(0)}}\right) + \sqrt{\gamma p_0}\left\{\frac{\partial p^{(2)}}{\partial x} + \rho^{(0)}\left(u^{(0)} + u_b\right)\frac{\partial u^{(0)}}{\partial x}\right\}\right)\right) + \mathrm{O}(M^2). \tag{31}$$

We observe that these amplitudes contain no acoustic components. This arises as a result of the assumption that the frozen solution is sufficiently evolved to be essentially acoustically quiescent. Acoustic quiescence in the frozen solution is not a necessary condition for the application of this approach; it is adopted here purely to simplify the algebra. The one remaining, outgoing amplitude (L_1) is calculated as part of the solution, and carries with it the outgoing acoustic behaviour. The shifting of the eigenvalues in Eqs. (29)–(31) by u_b arises as a result of the Galilean transformation applied to the frozen solution.

Using Eq. (7) for L_1, and Eqs. (29)–(31) for L_2–L_4, respectively, we find that the leading order terms in Eqs. (4a)–(4d) for the inflow boundary satisfy

$$\frac{\partial u^{(0)}}{\partial t} + u^{(0)}\frac{\partial u^{(0)}}{\partial x} + v^{(0)}\frac{\partial u^{(0)}}{\partial y} + \frac{1}{\rho^{(0)}}\frac{\partial p^{(2)}}{\partial x} = -\frac{1}{2\rho^{(0)}}\left(\frac{\partial p^{(1)}}{\partial \xi} - \sqrt{\gamma\rho^{(0)}p^{(0)}}\frac{\partial u^{(0)}}{\partial \xi}\right), \tag{32a}$$

$$\frac{\partial v^{(0)}}{\partial t} + u^{(0)}\frac{\partial v^{(0)}}{\partial x} + v^{(0)}\frac{\partial v^{(0)}}{\partial y} + \frac{1}{\rho^{(0)}}\frac{\partial p^{(2)}}{\partial y} = 0, \tag{32b}$$

$$\frac{\partial \rho^{(1)}}{\partial t} = -\frac{1}{2}\sqrt{\frac{\rho^{(0)}}{\gamma p^{(0)}}}\left(\frac{\partial p^{(1)}}{\partial \xi} - \sqrt{\gamma\rho^{(0)}p^{(0)}}\frac{\partial u^{(0)}}{\partial \xi}\right), \tag{32c}$$

$$\frac{\partial p^{(1)}}{\partial t} = -2\sqrt{\frac{\gamma p^{(0)}}{\rho^{(0)}}}\left(\frac{\partial p^{(1)}}{\partial \xi} - \sqrt{\gamma\rho^{(0)}p^{(0)}}\frac{\partial u^{(0)}}{\partial \xi}\right), \tag{32d}$$

$$\frac{\partial p^{(0)}}{\partial t} = \frac{\partial \rho^{(0)}}{\partial t} = 0. \tag{32e}$$

The acoustic terms on the right hand side of Eqs. (32a), (32c) and (32d) are provided purely by the outgoing amplitude. At the inlet boundary, the outgoing (i.e., leftward propagating) acoustic waves satisfy

$$\frac{\partial p^{(1)}}{\partial \xi} + \sqrt{\gamma \rho^{(0)} p^{(0)}} \frac{\partial u^{(0)}}{\partial \xi} = 0.$$

Substituting this condition into, say, Eq. (32a) gives

$$\frac{\partial u^{(0)}}{\partial t} + u^{(0)} \frac{\partial u^{(0)}}{\partial x} + v^{(0)} \frac{\partial u^{(0)}}{\partial y} + \frac{1}{\rho_0} \frac{\partial p^{(2)}}{\partial x} = \sqrt{\frac{\gamma p^{(0)}}{\rho^{(0)}}} \frac{\partial u^{(0)}}{\partial \xi},$$

demonstrating how the momentum equation correctly treats left-moving acoustic waves propagating at the local sound speed. Similar interpretations can be derived for Eqs. (32c) and (32d).

6.3. The final inflow condition

To reiterate: to impose non-reflecting inflow conditions, we calculate the incoming *amplitudes* from the frozen solution, while the remaining outgoing amplitude requires no modification.

7. Results

The boundary conditions described in this paper have been incorporated into a simulation code developed in-house at the University of Manchester. The code is based on a finite difference approach, and has been tested against a number of benchmark problems in order to accommodate the validation steps recommended by Roache [30,31]. The simulation software is a general compressible flow solver; it is able to work on either parallel or serial architectures and can, if required, deal with arbitrary reaction mechanisms and molecular transport. Time integration is achieved via a minimal storage, 3rd order Runge–Kutta method taken from the family described by Wray [32]. The code has a modular structure, and any one of a number of different numerical methods can be employed to suit a particular application. For the work described in this paper, the spatial discretization is performed using explicit 4th order schemes in both directions. Although not reported here, we have tried the boundary conditions in conjunction with schemes ranging from 2nd order explicit finite differences to 6th order compact methods. The results we obtained for each of these numerical schemes remain qualitatively the same as those reported here, although the overall accuracy of the solution diminishes for the lower order explicit schemes.

We have also observed that the different spectral responses of the numerical schemes (particularly in the boundary operators) have an effect on the pressure field, especially when simulating broad band spectra typical of turbulence. Rowley and Colonius [5] have analyzed the effect of numerical discretization on the linearized Euler equations but, for general turbulent flows, the effect of the boundary operators on the accuracy (as well as the stability) of the solution has not been extensively reported. The influence of the boundary operator on the pressure field is lessened in buffer layer treatments (where the last node of the physical domain does not coincide with the edge of the full computational domain). In flows with no such layer, boundary resolution and spectral response becomes more important. The spectral performance of a wide range of numerical schemes in the context of turbulence, and in conjunction with the new boundary conditions, will be described in a future paper.

For the test problems considered, the flow geometry comprises a two dimensional square grid spanning a distance of 10 mm in both spatial directions. For the single vortex and turbulent flow cases, the grid resolution is set at 128×128 points. For the twin vortex problem, we found that the thin structures evolving in the layer between the vortices are too small to resolve accurately with this resolution. Hence, the twin vortex problem is defined on a grid of 256×256 grid points. Periodic boundary conditions are imposed in the spanwise direction throughout. For the inflow/outflow directions, the new boundary conditions are imposed. As a basis for comparison, alternative calculations were also undertaken; in each case, these calculations were started from the same initial conditions, but used alternative non-reflecting criteria for the inflow/outflow directions. The new boundary conditions are hence tested against characteristics based (quasi one dimensional) boundary conditions [7,11,6], and the mixed 1st/4th order boundary conditions of Giles [6].

It is well known that nonreflecting boundary conditions typically reflect two types of waves: p and q waves [33,11]. The p waves are so named because they represent a reflection of the *physical* wave and typically comprise low wavelength phenomena. The q waves are spurious high frequency waves generated by the boundary conditions and the numerical scheme. The propagation of the p waves is governed by the physics of the flow, but the propagation of the q waves is controlled by their group velocity. As the q waves' propagation is not governed by the flow physics, they can propagate upstream regardless of the mean flow velocity. Consequently, it is the q waves that typically lead to numerical instability. To test the reflective properties of the new boundary conditions a right-going pressure pulse, defined as

$$p' = 10 \exp\left(-225 \times 10^4 \left(x - 5 \times 10^{-3}\right)^2\right)$$

was given as an initial condition. The pulse was allowed to propagate out of the domain via the new non-reflecting conditions. Defining the maximum amplitude of the outgoing pulse as A_1, we found that $A_p/A_1 \simeq 10^{-4}$ and $A_q/A_1 \simeq 10^{-6}$, where A_p is the physical wave reflection and A_q is the numerical wave reflection. These figures are consistent with other tests of characteristic boundary conditions [11].

7.1. Single vortex problem

The first flow configuration to be considered is that of a compressible, inviscid vortex. The vortex is defined in terms of the streamfunction as [11]

$$\psi = C \exp\left(-\frac{r^2}{2r_v^2}\right) + u_b y, \tag{33}$$

where C is the vortex strength, r is the radius and r_v is a characteristic length scale for the vortex. The mean flow speed in the x-direction is set via the inclusion of the u_b term. In a frame of reference attached to the vortex, the tangential and radial velocity distributions are given by

$$\begin{aligned} u_r &= 0, \\ u_\theta &= \frac{Cr}{r_v^2} \exp\left(-\frac{r^2}{2r_v^2}\right). \end{aligned} \tag{34}$$

Colonius et al. [34] have shown that such a vortex must have a radial pressure distribution that satisfies

$$\frac{\partial p}{\partial r} = \frac{\rho u_\theta^2}{r}. \tag{35}$$

If we assume that the flow has a constant speed of sound, equations for the density and pressure distributions can be derived as:

$$p(r) = p_\infty \exp\left(-\frac{\gamma}{2}\left(\frac{C}{ar_v}\right)^2 \exp\left(-\frac{r^2}{r_v^2}\right)\right),$$
$$\rho(r) = \rho_\infty \exp\left(-\frac{1}{2}\left(\frac{C}{ar_v}\right)^2 \exp\left(-\frac{r^2}{r_v^2}\right)\right), \tag{36}$$

and a vorticity distribution given by

$$\omega(r) = 2C\left(\frac{2r_v^2 - r^2}{r_v^4}\right)\exp\left(-\frac{r^2}{2r_v^2}\right).$$

In the following tests, the analytic expressions for the tangential velocity, the radial pressure gradient and the vorticity will be used as benchmarks. To quantify the performance of the new boundary conditions, a normalized error measure is introduced as

$$\frac{\|\phi(r,t) - \phi_a(r,t)\|_2}{\|\phi_a(r,0)\|_2}, \tag{37}$$

where r is the radius and $\|\phi\|_2 \equiv (\sum_{i,j}\phi_{i,j}^2)^{\frac{1}{2}}$. ϕ is taken as one of the quantities u_θ, $\partial p/\partial r$ or ω, the subscripts i,j refer to the grid position and the subscript a is used to denote analytic quantities. Eq. (37) is evaluated for each quantity in the polar reference frame attached to the vortex. These measures were chosen for this case firstly

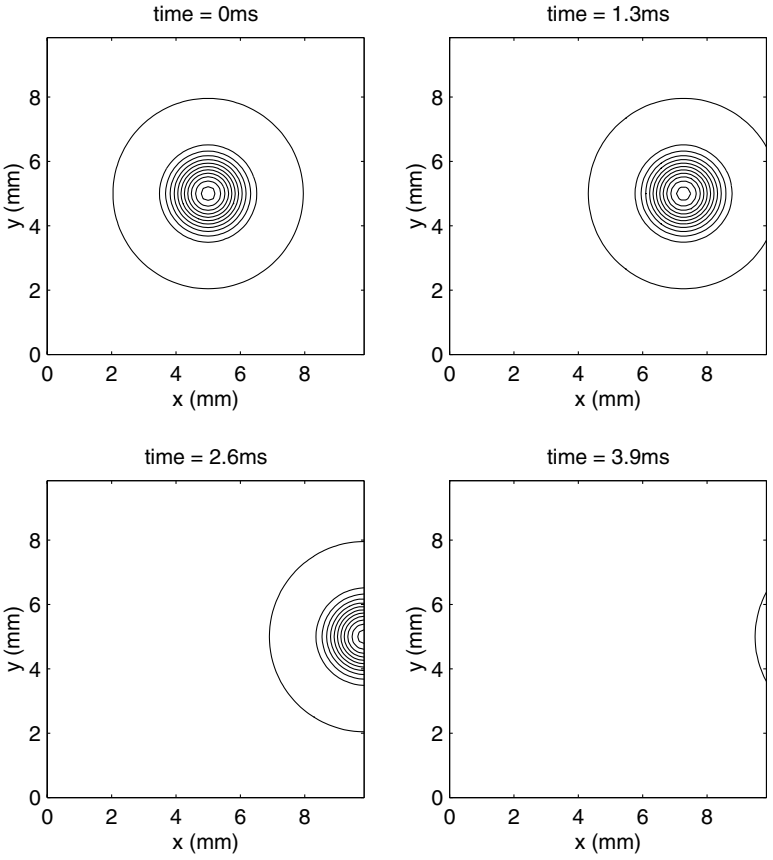

Fig. 4. Vorticity contours for single vortex problem using new boundary conditions.

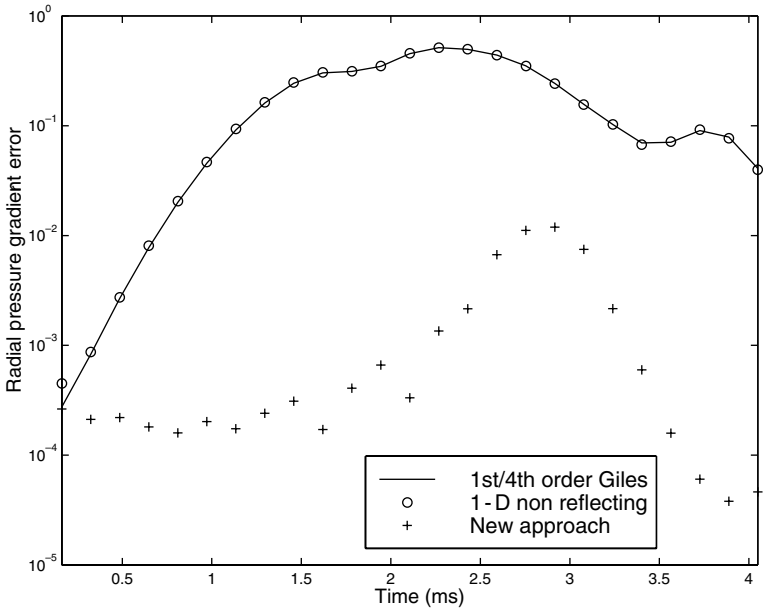

Fig. 5. Evolution of radial pressure gradient error with time. Single vortex case.

because the pressure has been found to be extremely sensitive to the choice of boundary treatment, and because u_θ and ω provide information about the flow distortion in directions normal and parallel to the boundary.

For the initial conditions, the mean flow speed in Eq. (33) is set at 2 m/s, the vortex strength is defined as 5×10^{-3} m^2/s and its characteristic radius is set at 10% of the domain size. The flow configuration and the initial conditions for this problem are essentially the same as those used to derive the solution shown in Figs. 1(a)–(d), but with the non-reflecting boundary conditions now replaced by the revised conditions derived in this paper.

Fig. 4 shows a series of vorticity contour plots obtained using the new boundary conditions. Figs. 5–7 show the evolution of the pressure gradient error, the tangential velocity error and the vorticity error, respectively, as the vortex traverses the boundary. The trends in all three families of curves are broadly similar: the new boundary conditions typically reduce the observed errors by between one and two orders of magnitude. For this particular flow configuration, the 1st/4th order treatment does not offer significant improvements on the first order one dimensional approximation. This finding is consistent with Giles [6] (who attributed the error to numerical truncation), and with Colonius et al. [34], who circumvented the problem via the inclusion of a buffer layer at the outflow. The new treatment appears to require no such layer.

7.2. Co-rotating vortices

The second case to be considered is that of two co-rotating vortices. This test case is chosen because the flow field exhibits unsteadiness in the inertial length scales. The flow field is initialized with two vortices defined by the streamfunction

$$\psi = C\left(\exp\left(-\frac{r_1^2}{2r_v^2}\right) + \exp\left(-\frac{r_2^2}{2r_v^2}\right)\right) + u_b y,$$

$$r_1 = (x-\xi)^2 + (y+\delta)^2,$$

$$r_2 = (x-\xi)^2 + (y-\delta)^2.$$

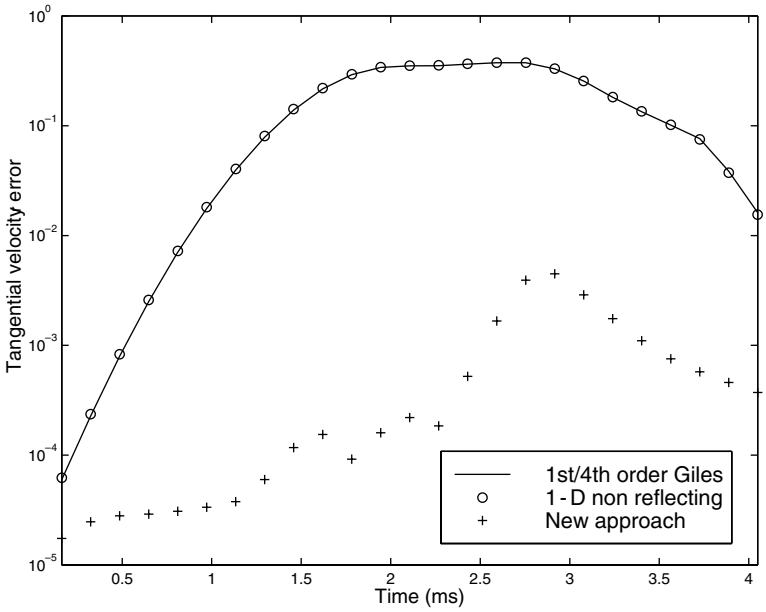

Fig. 6. Evolution of tangential velocity error with time. Single vortex case.

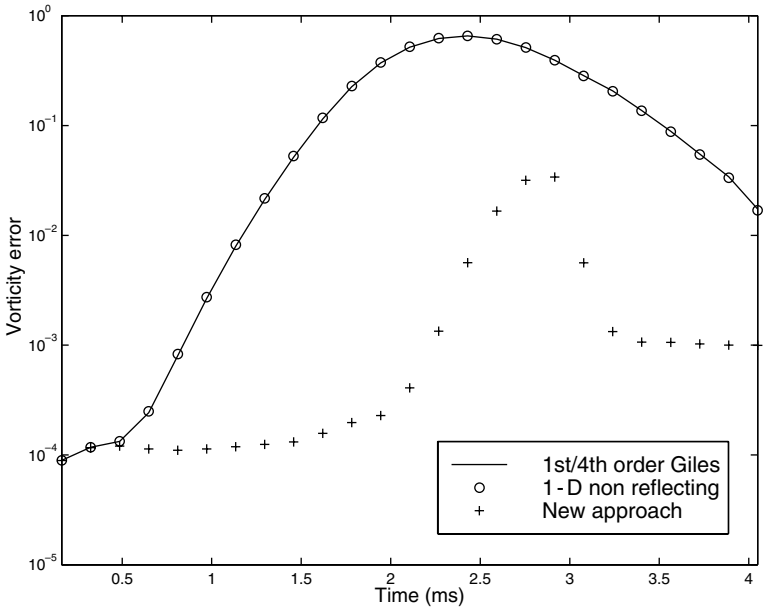

Fig. 7. Vorticity error history. Single vortex problem.

For these simulations, r_v and δ were set to 10% and 15% of the transverse domain size, respectively. The horizontal offset ξ was set at 35% of the domain size, and was chosen to reduce the time taken for the vortices to reach the outflow boundary. The vortices' strengths were each set at 1.25×10^{-3} m/s^2 and

the freestream velocity was set at 0.5 m/s. The combination of low freestream velocity with two comparatively intense vortices leads to local flow reversals in the vortex pair, and is a particularly stringent test of the boundary conditions. In those parts of the outflow where there are local flow reversals, the normal non-reflecting practise is adopted for the vorticity and entropy waves; only the incoming acoustic mode is specified via the new boundary condition.

The initial velocity, pressure and density fields were calculated from a superposition of two independent vortex solutions. This produced an initial acoustic transient, the transverse component of which has no dissipative component and reflects repeatedly due to the assumption of spanwise periodicity. Initial tests revealed that the magnitude of this transient is less than the pressure drop induced by the vortical structures. These same tests also revealed that the use of an error measure based on pressure *gradients* is unduly influenced by the transverse acoustics and clouds the errors arising from the outflow boundaries alone. Consequently, we do not use pressure gradient as an appropriate measure for this test case.

There are no closed form analytic solutions for this problem. To obtain a benchmark solution, a reference simulation was undertaken with a streamwise flow domain size twice that of the test problems. One dimensional non-reflecting conditions were used for the outlet boundary conditions, and a fixed velocity non-reflecting condition was specified for the inflow. The initial conditions resulted in a steady, uniform flow field near both boundaries for the benchmark solution, and the simulation was stopped long before the vortex pair reached the outflow. A virtual plane was inserted at the half way point in the augmented simulation; this coincided with the outflow boundary of the test problems. The error measures used the left half of the augmented domain as the reference solution. The evolution of the benchmark solution in the left half of the domain is shown in Fig. 8; Fig. 9 depicts the time history of the normalized vorticity in the same region.

For this problem, error norms for vorticity and absolute pressure were used:

$$\frac{\left\|\omega(\mathbf{x},t)-\omega(\mathbf{x},t)_{\mathrm{ref}}\right\|_2}{\left\|\omega(\mathbf{x},0)_{\mathrm{ref}}\right\|_2},$$

$$\frac{\left\|p(\mathbf{x},t)-p(\mathbf{x},t)_{\mathrm{ref}}\right\|_2}{\left\|p(\mathbf{x},0)_{\mathrm{ref}}-p^{(0)}\right\|_2},$$

where the 2-norms are defined in the same sense as in the previous section, and $p^{(0)}$ is the leading order (thermodynamic) pressure, defined as 101325 N/m^2. The quantities with the suffix 'ref' were obtained from the left half of the benchmark solution. We note that the transverse acoustic waves present in this solution represent the worst case scenario for the new approach, because the revised boundary conditions do tend to distort acoustic waves that propagate normal to the boundary. This is because in these cases, the assumption used to specify $u_\xi^{(0)}$ (i.e., the waves approach the boundary normally), is inaccurate. Future work will examine numerically accurate methods of partitioning more accurately the acoustic perturbations into the individual $u_\xi^{(0)}$ and $v_\theta^{(0)}$ terms.

The time dependence of the error measures is provided in Figs. 10 and 11. Again, it can be seen that the new approach yields significant reductions in the discrepancies between the benchmark and test simulations. For the 1-D boundary conditions, a transverse pressure mode is set up by the interaction of the vortex system with the boundary. These continue to reflect in the transverse direction due to the periodicity in that direction, and produce the sawtooth wave visible in Fig. 10. Interestingly, the 1st/4th order boundary conditions perform considerably better in this test. Initially, the error in the pressure field is an order of magnitude greater than that of the new boundary conditions. After approximately 3 ms, this error reduces to between 2 and 5 times that of the new boundary conditions.

The vorticity error histories in Fig. 11 show that initially large differences between the solutions reduce considerably at a simulation time of 5 ms. We believe that the similarity between the results here

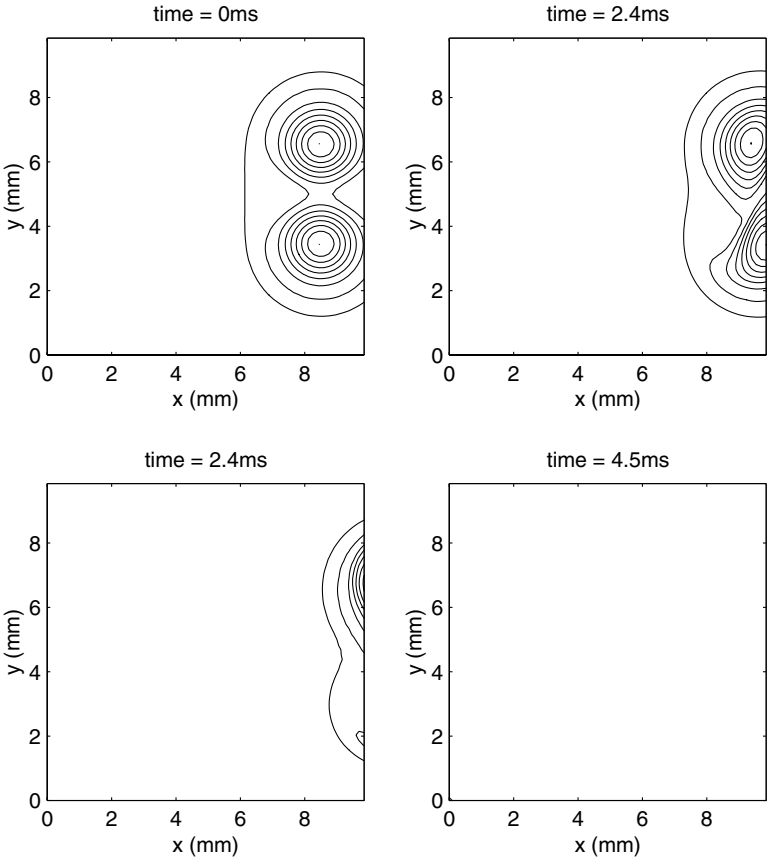

Fig. 8. Vorticity contours for twin vortex problem.

stems from the identical treatment of the vorticity and entropy waves by all of the boundary conditions. While the vortices are close to the boundary (but not crossing it), the one-dimensional and 1st/4th order boundary conditions produce a spurious incoming acoustic mode that alters the subsequent evolution of the flow. As the vortices cross the boundary, the solution accuracy appears to be additionally governed by both the entropy and vorticity waves. At around the 5 ms mark, local flow reversals are induced by the vorticity. In these local inflow regions, all of the non-reflecting conditions considered here specify zero incoming vorticity. This clearly is not the correct boundary condition, and the subsequent reduction of accuracy demonstrates this. The idea that the error is related to the vorticity wave treatment is substantiated by the fact that the distortion of the vortical structures is localized to the region of the boundary; if the acoustic mode were to blame, we might expect vorticity production to occur over the whole flow domain.

7.3. Two dimensional inviscid turbulence

The final problem to be studied is that of two-dimensional turbulence. The initial conditions for this flow were generated using the methods described by Rogallo [35]. The turbulent velocity fluctuations were calculated such that the resultant energy spectrum satisfied [36]

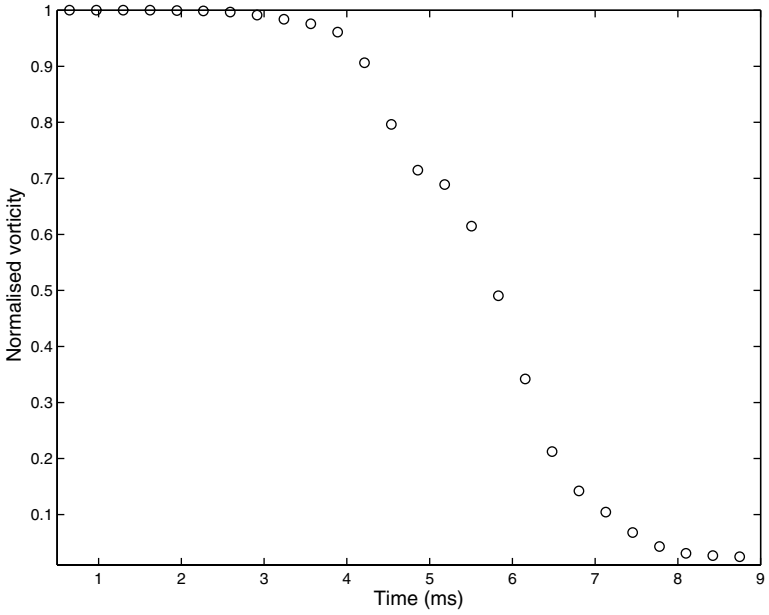

Fig. 9. Normalised vorticity history for twin vortex problem.

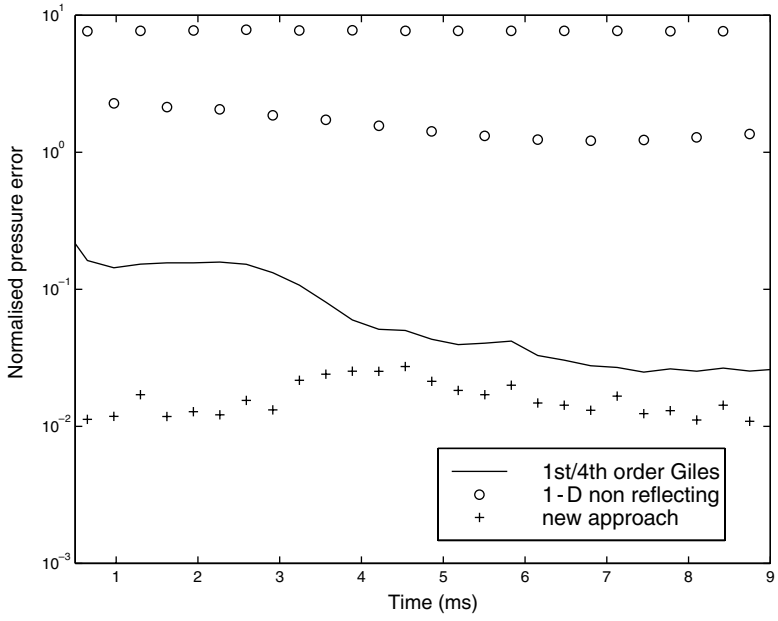

Fig. 10. Normalised pressure error for twin vortex problem.

$$E(k) = \begin{cases} \frac{72}{\pi}\frac{k}{k^4+6^4} & k \leqslant k_{\max}, \\ 0 & k \geqslant k_{\max}, \end{cases}$$

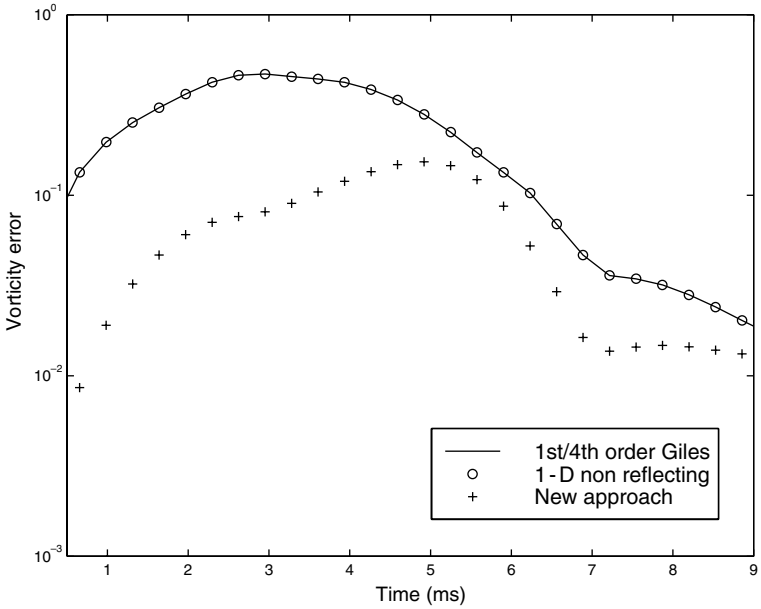

Fig. 11. Normalised vorticity error for twin vortex problem.

$k_{\max}$ was set for this study at 12; a subsequent normalization of the energy spectrum produced a turbulence rms intensity of 0.1 m/s (5% of the mean flow speed for this case). The resultant flow field contains a range of length and time scales characteristic of turbulence, but one that is readily resolved using a low resolution grid of 128×128 grid points. This last comment is particularly aimed at the one sided schemes used at the inflow/outflow boundaries; these often have a lower formal order of accuracy, and a much poorer spectral resolution, than symmetric internal constructions. The mean velocity for this investigation was set at 2 m/s and the physical size of the domain was set at 10 mm × 10 mm.

The flow was simulated for 1 convective flow time ($\sim l_0/u_0 = 5$ ms), during which we established the long term stability of the new boundary conditions. For each of the different boundary conditions used, the rms pressure, vorticity and kinetic energy were monitored throughout the simulation, where (for example)

$$p_{\mathrm{rms}}(t) = \sqrt{\frac{\sum_{i,j}\left(p_{i,j}(t) - p^{(0)}\right)^2}{N_i N_j}},$$

N_i, N_j are the number of grid cells in the x- and y-directions, respectively, and the suffices i,j refer to grid points. As the flow is inviscid and two dimensional, the vorticity should be conserved. Similarly, the absence of mean shear and a dissipative mechanism implies that the kinetic energy, and therefore the fluctuating pressure, should also remain statistically steady [26]. The history of $p_{\mathrm{rms}}(t)$, normalized by $p_{\mathrm{rms}}(0)$, is presented in Fig. 12. We found that the pressure remained essentially constant and O(1) for the new boundary conditions, while it varied significantly for the simulations with the quasi one dimensional boundary conditions and the 1st/4th order boundary conditions. In contrast, the rms statistics of the vorticity and kinetic energy appeared to have the correct statistically steady behaviour, and remained O(1) during the simulation, regardless of the boundary condition chosen. It seems that, while using the one-dimensional and 1st/4th order boundary conditions induces a large pressure perturbation, the perturbation is *rapidly fluctuating*. Consequently, the *net* effect on the flow field is smaller than the instantaneous pressure variation might suggest.

To test the non-reflecting character of both the inflow and outflow boundaries in the presence of turbulence, the pressure field associated with the initial conditions described above was modified via the inclusion of an additional pressure pulse. The pressure pulse was planar, with normals parallel to the mean flow and located midway between the inlet and outlet. The perturbation was the same as that used to derive the reflection coefficients:

$$p' = 10\exp\left(-225\times 10^4\left(x-5\times 10^{-3}\right)^2\right). \tag{38}$$

This perturbation is about 2 orders of magnitude larger than that expected from the dynamic field alone. The pressure distribution for the initial flow field is shown in Fig. 13. Note that the white region in the center of the plot corresponds to a *large* excursion from the mean value; the contour plot has been clipped in order retain the visibility of the small pressure perturbations induced by the turbulence.

The simulation was run twice. The first simulation evolved from the set of initial conditions *without* the pressure pulse, and provided the evolving benchmark pressure field $p_{\mathrm{ref}}(\mathbf{x},t)$. The second simulation shared the same inertial features as the benchmark solution, but also included the pressure perturbation given by Eq. (38). The idea is that the two simulations should share the same time dependent inertial behaviour, but the second simulation should have an additional acoustic component. If the non-reflecting boundary conditions work correctly, this component should leave the domain after half an acoustic transit time (defined as $l_0/a_0 \sim 28$ μs using the data in this paper). The two solutions should thereafter evolve identically, and the difference between them, embodied by the normalized pressure difference

$$\frac{\|p(\mathbf{x},t)-p_{\mathrm{ref}}(\mathbf{x},t)\|_2}{\|p(\mathbf{x},t_0)-p^{(0)}\|_2} \tag{39}$$

should vanish.

Fig. 14 shows a logarithmic plot of the time history of the normalized pressure difference (Eq. (39)). It can be seen that by $t = 5$ μs, the initial single pressure pulse has split into two smaller waves; this accounts

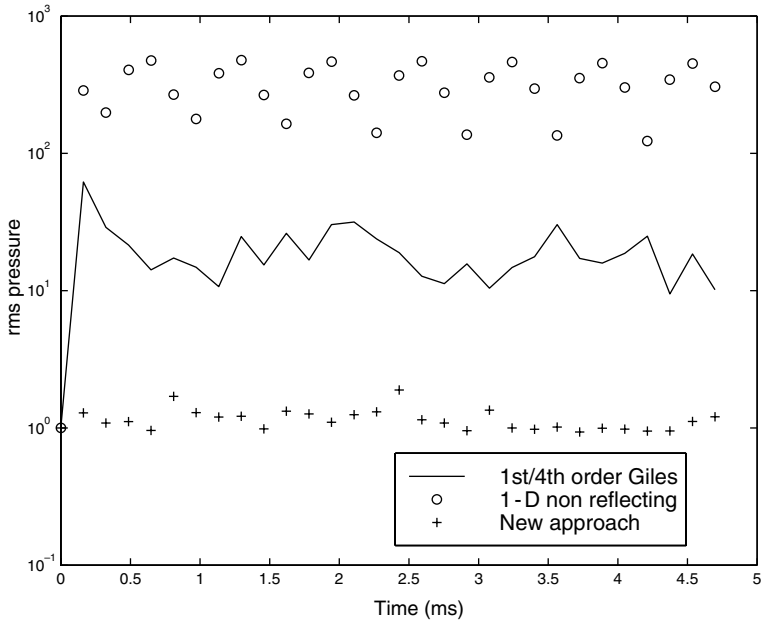

Fig. 12. Normalised rms pressure for turbulent flow.

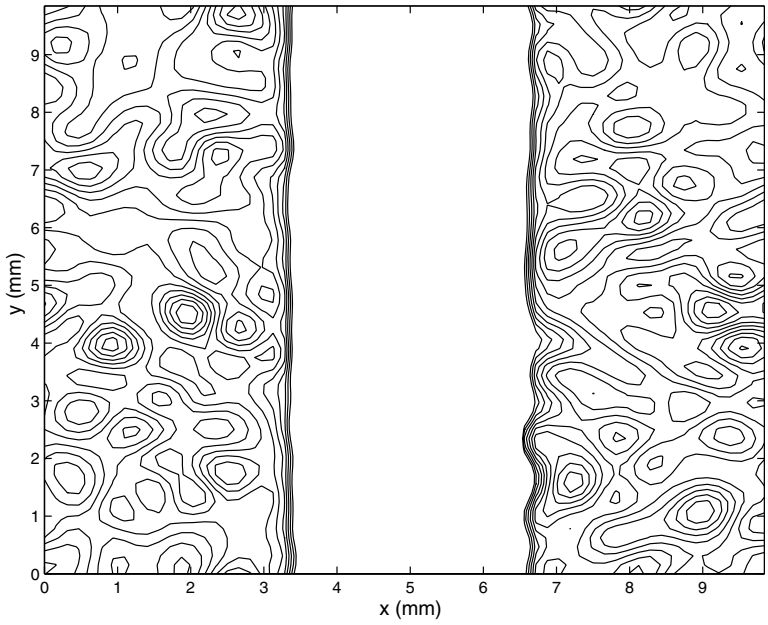

Fig. 13. Initial conditions for turbulent flow with central pressure pulse.

for the reduction in normalized pressure difference in the figure. The waves begin to leave the domain at around $t = 14$ μs, whereupon the difference between the two solutions drop by 3 orders of magnitude, corresponding to a reflection of about 0.1%. After a further acoustic transit time, there is an additional reduction in the difference between the two solutions. By the time $t = 80$ μs is reached, the normalized difference between the two solutions is approximately 0.01%. We note that, using the nomenclature of previous sections, this reflection corresponds to $A_p/A_1 \simeq 10^{-3}$, which is larger than for the reflection test with a steady flow field. It is not immediately clear why this reflection is larger; we believe that it may stem either from the numerical schemes' difficulty in resolving simultaneously the spectrum of the turbulence and the acoustic wave, or alternatively from the inflow boundary conditions, where there is a time discontinuous evolution of the flow field. Regardless, the performance of the method still appears satisfactory.

The simulations were allowed to continue to run for an additional 45×10^3 time steps, which corresponds to just over 1 flow transit time through the domain. At the end of this extended run, no significant errors in the pressure field are observed; the dynamic pressure variations remained bounded essentially by the kinetic energy of the turbulence.

Fig. 15 shows the time history of the normalised pressure difference for a simulation with a mean flow speed of Mach 1.5 (≃520 m/s). This simulation was performed to verify that the Mach number perturbations used to derive the boundary conditions do not break down for $M \geqslant 1$. The high flow speed in this case results in all of the eigenvalues being positive. Consequently, even the upstream running wave (associated with $\lambda_1 = (u - a)$) propagates rightward through the outflow boundary.

It can be seen from Fig. 15 that the acoustic wave associated with the downstream running amplitude leaves the domain within 10 μs of the start of the simulation. Similarly, the upstream running waves leaves the domain between 40 and 50 μs after the start of the simulation. Once the initial transients have left, the normalised pressure difference drops to about 0.4% of its initial starting value; this is a similar value to that encountered in the low mean speed flow case.

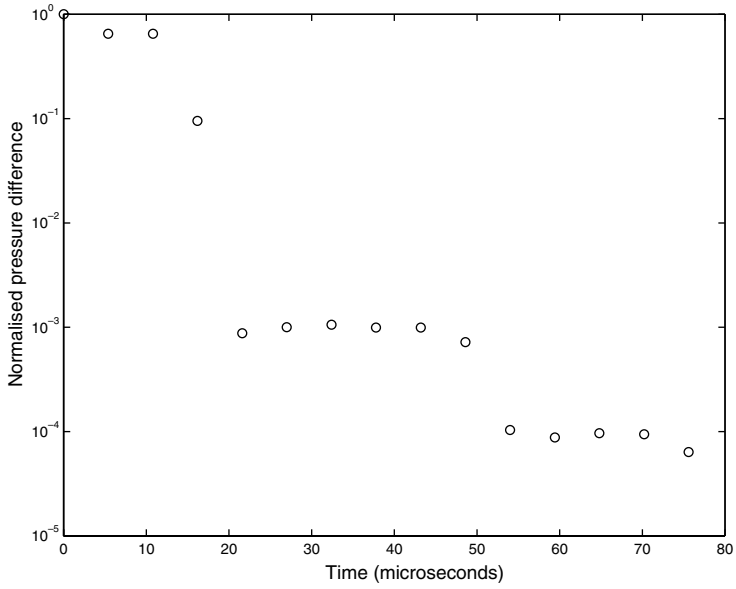

Fig. 14. Evolution of normalised pressure difference $\|p(x,t) - p_{\mathrm{ref}}(\mathbf{x},t)\|_2 / \|p(x,t_0) - p^{(0)}\|_2$ for turbulent flow.

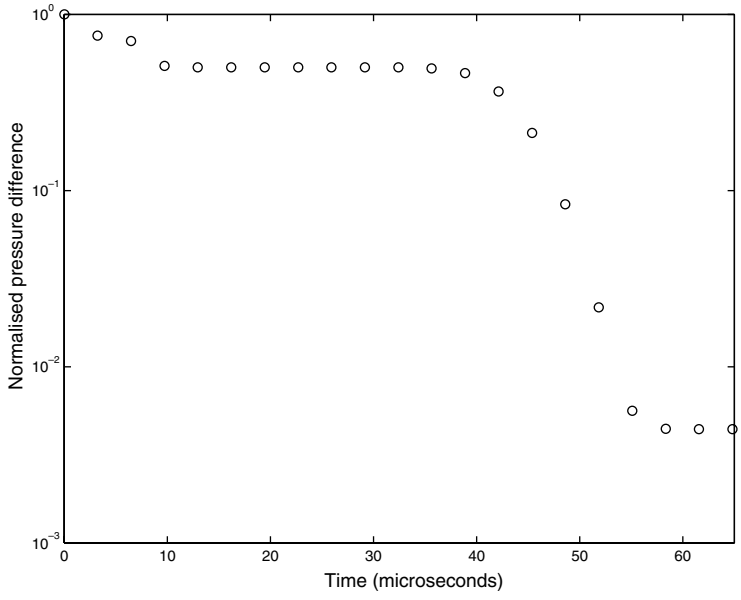

Fig. 15. Evolution of normalised pressure difference $\|p(x,t) - p_{\mathrm{ref}}(\mathbf{x},t)\|_2 / \|p(\mathbf{x},t_0) - p^{(0)}\|_2$ for turbulent flow with a mean flow Mach number of $M = 1.5$.

7.4. Obliquely propagating waves

The performance of the new approach was examined for waves propagating obliquely to the outflow boundary. For this, three further simulations were undertaken, in which Eq. (38) was used to provide a

rightward propagating pressure wave that moved through an essentially stagnant flow field. For each simulation, the pressure pulse was rotated to give a different angle of incidence, α. The angles of incidence, measured relative to the x-axis, were set at 22.5°, 45°, and 67.5°, respectively.

The quality of the solutions was expressed by a normalized pressure difference

$$\frac{\left\|p(\mathbf{x}_b,t)-p^{(0)}\right\|_\infty}{\left\|p(\mathbf{x}_b,0)-p^{(0)}\right\|_\infty}, \tag{40}$$

where $\mathbf{x}_b$ is a location along the outflow boundary. We have adopted ∞-normalization here because we found that the structure of the acoustic wave distorts non-uniformly as it crosses the outflow boundary. If the simulation is perfect, the error measure given by Eq. (40) should have an initial value of 1, and decrease monotonically to zero as the wave leaves the domain through the top right hand corner of the domain.

Figs. 16–18 show the performance of the new boundary conditions in comparison to quasi one dimensional boundary conditions. It can be seen that the new approach suffers from similar problems to the one dimensional approach when the wave approaches the boundary obliquely. In particular, we note that pressure waves approaching the boundary at higher angles of incidence suffer from an artificial reduction in the acoustic pressure, and this reduction is larger than that incurred when using quasi one dimensional boundary conditions. The reason for this stems from the manner in which the acoustically driven velocity gradients are calculated. We have seen in the previous sections that $\partial u^{(0)}/\partial\xi$ is essentially equated to the divergence of the flow field. Clearly, such an approach cannot discriminate between normally approaching waves and waves approaching at an angle (where the divergence has two components; $\partial u^{(0)}/\partial\xi$ and $\partial v^{(0)}/\partial\theta$). As the angle of the wave increases with respect to the outflow, the majority of the acoustic divergence should more properly be accounted for by the $\partial v^{(0)}/\partial\theta$ term. At present there appears to be no robust method for the partitioning of the acoustic divergence into normal and transverse components; methods to calculate the propagation direction based on the gradients of the divergence are numerically ill behaved. Future work will look toward improving this situation.

Despite this drawback, we note that for the angles of incidence considered, the performance of the new boundary conditions is at least comparable to the quasi one dimensional approach.

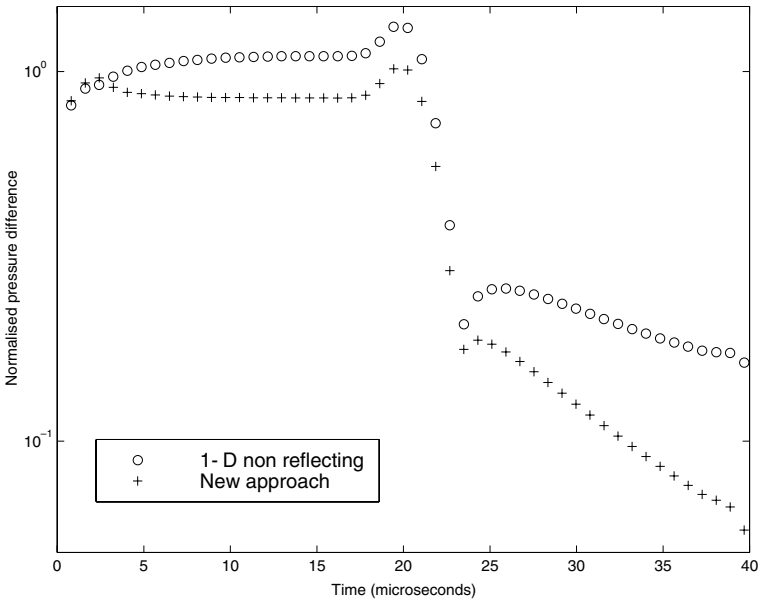

Fig. 16. Time evolution of normalised pressure difference. $\alpha = 22.5°$ case.

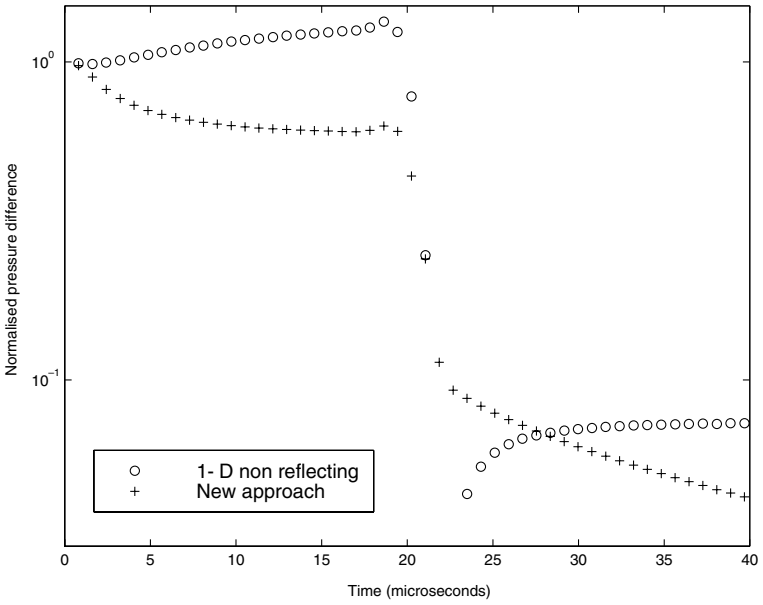

Fig. 17. Time evolution of normalised pressure difference. $\alpha = 45°$ case.

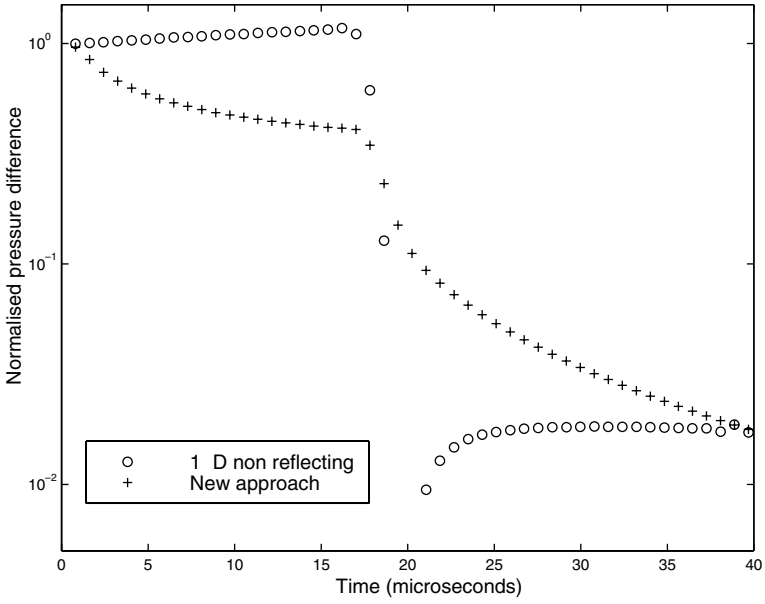

Fig. 18. Time evolution of normalised pressure difference. $\alpha = 67.5°$ case.

8. Conclusions

We have presented asymptotic expansions of the characteristic amplitudes used to develop non-reflecting boundary conditions. By matching terms, we have shown that the classical non-reflecting boundary condition is best applied to flows without significant inertial phenomena. Modifications have been proposed that

allow turbulent flow structures to be convected into or out of the domain, while retaining acoustic transparency. The new approach is at least as transparent to acoustic waves as the classical approach. Components of the incoming characteristics are retained in the new approach, so proving the stability of the scheme is difficult. Numerical experiments have however shown that the scheme is stable for long integration times. The generalization of the approach to 3 spatial dimensions is straightforward (Eqs. (26a), (26b), and (27) simply need to be revised to include additional transverse terms).

The proposed boundary conditions have shown themselves to behave well both at low and high Mach numbers. The new conditions suffer from a reduction in performance when the acoustic waves approach the boundaries at an angle. Future work will seek to remedy this problem.

The low Mach number expansions used in this paper provide an elegant means of coupling viscous effects into the boundary conditions. Chemical reactions may also be accommodated, as spatially varying species mass fractions provide a purely leading order modification to the analyses presented here. Both viscous and chemically reacting flows will be addressed in a forthcoming paper.

Acknowledgement

The author gratefully acknowledges Dr. R.S. Cant and the referees for their helpful comments regarding draft versions of this manuscript.

Appendix A. Low Mach number expansions

We consider the dimensionless Euler equations, and assume that they can be decomposed into two characteristic length scale ranges, denoted by (x,y) and (ξ,θ), with $\xi = Mx$ and $\theta = My$. ξ and θ are referred to as acoustic length scales and (x,y) are referred to as 'inertial' length scales. Using these assumptions, derivatives appearing in the original Euler equations are re-expressed as

$$\begin{aligned}\left.\frac{\partial}{\partial\widetilde{x}}\right|_{M,t} &= \frac{\partial}{\partial x} + M\frac{\partial}{\partial\xi},\\ \left.\frac{\partial}{\partial\widetilde{y}}\right|_{M,t} &= \frac{\partial}{\partial y} + M\frac{\partial}{\partial\theta}.\end{aligned} \tag{A.1}$$

Substituting the two scale derivatives back into the Euler equations, we obtain a power series in terms of the characteristic flow Mach number. The leading order momentum equations are

$$\begin{aligned}&\frac{\partial p^{(0)}}{\partial x} = \frac{\partial p^{(0)}}{\partial y} = 0,\\ &\frac{\partial p^{(1)}}{\partial x} = \frac{\partial p^{(1)}}{\partial y} = 0,\\ &\frac{\partial p^{(0)}}{\partial \xi} = \frac{\partial p^{(0)}}{\partial \theta} = 0,\\ &\frac{\partial u^{(0)}}{\partial t} + u^{(0)}\frac{\partial u^{(0)}}{\partial x} + v^{(0)}\frac{\partial u^{(0)}}{\partial y} + \frac{1}{\rho^{(0)}}\left(\frac{\partial p^{(2)}}{\partial x} + \frac{\partial p^{(1)}}{\partial \xi}\right) = 0,\\ &\frac{\partial v^{(0)}}{\partial t} + u^{(0)}\frac{\partial v^{(0)}}{\partial x} + v^{(0)}\frac{\partial v^{(0)}}{\partial y} + \frac{1}{\rho^{(0)}}\left(\frac{\partial p^{(2)}}{\partial y} + \frac{\partial p^{(1)}}{\partial \theta}\right) = 0.\end{aligned} \tag{A.2}$$

From the above set of equations, it follows that $p^{(0)} = \text{const.}$ and that $p^{(1)} = p^{(1)}(\xi,\theta)$.

The energy equation is written here in terms of the pressure transport equation. Using the same approach as that adopted for the momentum equation, we obtain

$$\begin{aligned}
&\frac{\partial p^{(0)}}{\partial t} + \gamma p^{(0)}\left(\frac{\partial u^{(0)}}{\partial x} + \frac{\partial v^{(0)}}{\partial y}\right) = 0,\\
&\frac{\partial p^{(1)}}{\partial t} + \gamma p^{(0)}\left(\frac{\partial u^{(1)}}{\partial x} + \frac{\partial v^{(1)}}{\partial y} + \frac{\partial u^{(0)}}{\partial \xi} + \frac{\partial v^{(0)}}{\partial \theta}\right) + \gamma p^{(1)}\left(\frac{\partial u^{(0)}}{\partial x} + \frac{\partial v^{(0)}}{\partial y}\right) = 0.
\end{aligned} \tag{A.3}$$

For flows on open domains, the thermodynamic pressure is constant in time and space, i.e., there is no bulk compression. It follows that

$$\begin{aligned}
&\frac{\partial u^{(0)}}{\partial x} + \frac{\partial v^{(0)}}{\partial y} = 0,\\
&\frac{\partial p^{(1)}}{\partial t} + \gamma p^{(0)}\left(\frac{\partial u^{(1)}}{\partial x} + \frac{\partial v^{(1)}}{\partial y} + \frac{\partial u^{(0)}}{\partial \xi} + \frac{\partial v^{(0)}}{\partial \theta}\right) = 0.
\end{aligned} \tag{A.4}$$

Finally, if p^1 is to be a function of the acoustic length scales alone, then

$$\frac{\partial u^{(1)}}{\partial x} + \frac{\partial v^{(1)}}{\partial y} = 0 \tag{A.5}$$

and

$$\frac{\partial p^{(1)}}{\partial t} + \gamma p^{(0)}\left(\frac{\partial u^{(0)}}{\partial \xi} + \frac{\partial v^{(0)}}{\partial \theta}\right) = 0. \tag{A.6}$$

To simplify the continuity equation, we recall the definition of the thermodynamic entropy for a divariant gas:

$$\mathrm{d}s = c_v \frac{\mathrm{d}p}{p} - c_p \frac{\mathrm{d}\rho}{\rho}. \tag{A.7}$$

Given that the flow is isentropic to all orders, it follows that

$$\begin{aligned}
&\frac{\partial \rho^{(0)}}{\partial x} = \frac{\partial \rho^{(0)}}{\partial y} = 0,\\
&\frac{\partial \rho^{(0)}}{\partial \xi} = \frac{\partial \rho^{(0)}}{\partial \theta} = 0,\\
&\frac{\partial \rho^{(1)}}{\partial x} = \frac{\partial \rho^{(1)}}{\partial y} = 0,\\
&\frac{\partial \rho^{(1)}}{\partial t} + \rho^{(0)}\left(\frac{\partial u^{(0)}}{\partial \xi} + \frac{\partial v^{(0)}}{\partial \theta}\right) = 0.
\end{aligned} \tag{A.8}$$

Appendix B. Obtaining the characteristics of the Euler equations

Omitting the transverse terms from Eqs. (3a)–(3d), the one-dimensional Euler equations are written as

$$\frac{\partial}{\partial t}(\mathbf{U}) + \mathbf{A}\frac{\partial}{\partial x}(\mathbf{U}) = 0, \tag{B.1}$$

where

$$\mathbf{A} = \begin{pmatrix} u & \rho & 0 & 0 \\ 0 & u & 0 & \frac{1}{\rho} \\ 0 & 0 & u & 0 \\ 0 & \gamma p & 0 & u \end{pmatrix} \qquad \mathbf{U} = \begin{pmatrix} \rho \\ u \\ v \\ p \end{pmatrix}.$$

Extracting the eigenvalues and eigenvectors of **A** allows Eq. (B.1) to be re-written in terms of characteristic waves;

$$\mathbf{S}\frac{\partial}{\partial t}(\mathbf{U}) + \boldsymbol{\Lambda}\mathbf{S}\frac{\partial}{\partial x}(\mathbf{U}) = 0. \tag{B.2}$$

S is the matrix of left eigenvectors of **A** and $\boldsymbol{\Lambda}$ is the associated diagonal matrix consisting of the eigenvalues of **A**. The differential of the characteristic variables are defined as $\mathrm{d}\boldsymbol{\psi} = \mathbf{S}\mathrm{d}\mathbf{U}$, and hence Eq. (B.2) is written as the following set of wave equations;

$$\frac{\partial}{\partial t}(\boldsymbol{\psi}) + \boldsymbol{\Lambda}\frac{\partial}{\partial x}(\boldsymbol{\psi}) = 0. \tag{B.3}$$

Using the nomenclature of [11], Eq. (B.2) is written as

$$\mathbf{S}\frac{\partial}{\partial t}(\mathbf{U}) + \mathbf{L} = 0 \tag{B.4}$$

or, more often

$$\frac{\partial}{\partial t}(\mathbf{U}) + \mathbf{S}^{-1}\mathbf{L} = 0. \tag{B.5}$$

Eq. (B.5) is explicitly included in Eqs. (4a)–(4d), where the transverse terms have been re-introduced.

References

[1] G. Hedstrom, Nonreflecting boundary conditions for nonlinear hyperbolic systems, J. Comput. Phys. 30 (1979) 222–237.
[2] F. Grinstein, Open boundary conditions in the simulation of subsonic turbulent shear flows, J. Comput. Phys. 115 (1994) 43–55.
[3] S. Tsynkov, Numerical solution of problems on unbounded domains. A review, Appl. Numer. Math. 27 (1998) 465–532.
[4] B. Petersen, Introduction to the Fourier Transform and Pseudodifferential Operators, Pitman Advanced, London, 1983.
[5] C. Rowley, T. Colonius, Discretely nonreflecting boundary conditions for linear hyperbolic systems, J. Comput. Phys. 157 (2000) 500–538.
[6] M. Giles, Nonreflecting boundary conditions for Euler equation calculations, AIAA J. 28 (1990) 2050–2058.
[7] K. Thompson, Time dependent boundary conditions for hyperbolic systems, J. Comput. Phys. 68 (1987) 1–24.
[8] R. Vichnevetsky, Invariance theorems concerning reflection at numerical boundaries, J. Comput. Phys 63 (1986) 268–282.
[9] D. Rudy, J. Strikwerda, Boundary conditions for subsonic compressible Navier–Stokes calculations, Comput. Fluids 9 (1981) 327–338.
[10] D. Rudy, J. Strikwerda, A nonreflecting outflow boundary condition for subsonic Navier–Stokes calculations, J. Comput. Phys. 36 (1980) 55–70.
[11] T. Poinsot, S. Lele, Boundary conditions for direct simulations of compressible viscous flows, J. Comput. Phys 101 (1992) 104–129.
[12] F. Nicoud, Defining wave amplitude in characteristic boundary conditions, J. Comput. Phys. 149 (1999) 418–422.
[13] M. Baum, T. Poinsot, D. Thévenin, Accurate boundary conditions for multicomponent reactive flows, J. Comput. Phys. 116 (1994) 247–261.
[14] D. Thevénin, M. Baum, T. Poinsot (Eds.), Direct Numerical Simulation for Turbulent Reacting Flows, Editions Technip, Paris, 1996.
[15] J. Sutherland, C. Kennedy, Improved boundary conditions for viscous, reacting, compressible flows, J. Comput. Phys. 191 (2003) 502–524.

[16] T. Colonius, S. Lele, P. Moin, Boundary conditions for direct computation of aerodynamic sound generation, AIAA J. 31 (1993) 1574–1582.
[17] J. Freund, Noise sources in a low-Reynolds-number turbulent jet at Mach 0.9, J. Fluid. Mech. 428 (2001) 277–305.
[18] T. Colonius, S. Lele, P. Moin, Sound generation in a mixing layer, J. Fluid Mech. 330 (1997) 375–409.
[19] B. Rembold, M. Adams, L. Kleiser, Direct numerical simulation of a transitional rectangular jet, Int. J. Heat Fluid Flow 23 (2002) 547–553.
[20] X. Jiang, K. Luo, Direct numerical simulation of the near field dynamics of a rectangular reactive plume, Int. J. Heat Fluid Flow 22 (2001) 633–642.
[21] X. Jiang, K. Luo, Direct numerical simulation of the puffing phenomenon of an axisymmetric thermal plume, Theoret. Comput. Fluid Dynamics 14 (2000) 55–74.
[22] F. Hu, On absorbing boundary conditions for linearized euler equations by a perfectly matched layer, J. Comput. Phys. 129 (1996) 201–219.
[23] F. Hu, A stable, perfectly matched layer for linearized Euler equations in unsplit physical variables, J. Comput. Phys. 173 (2001) 455–480.
[24] J. Hesthaven, On the analysis and construction of perfectly matched layers for the linearized Euler equations, J. Comput. Phys. 142 (1998) 129–147.
[25] K. Asato, H. Nagata, T. Kawamura, Extinction of premixed curved flames stabilized in a stagnation flow, in: A. Kuhl, J. Leyer, A. Borisov, W. Sirignano (Eds.), Dynamics of Deflagrations and Reactive Systems: Flames, AIAA, 1989, pp. 161–175.
[26] S. Pope, Turbulent Flows, Cambridge University Press, Cambridge, 2003.
[27] H. Yee, N. Sandham, M. Djomehri, Low-dissipative high-order shock-capturing methods using characteristic-based filters, J. Comput. Phys. 150 (1999) 199–238.
[28] P. McMurtry, W. Jou, J. Riley, R. Metcalfe, Direct numerical simulations of a reacting mixing layer with chemical heat release, AIAA 24 (1986) 962–970.
[29] R. Klein, Semi-implicit extension of a Godunov-type scheme based on low mach number asymptotics I: one dimensional flow, J. Comput. Phys. 121 (1995) 213–237.
[30] P. Roache, Quantification of uncertainty in CFD, Ann. Rev. Fluid Mech. 29 (1997) 123–160.
[31] P. Roache, Verification of codes and calculations, AIAA J. 36 (1998) 696–702.
[32] A. Wray, Minimal Storage Time-advancement Schemes for Spectral Methods, NASA Ames Research Center, 1990.
[33] R. Vichnevetsky, J. Bowles, Fourier Analysis of Numerical Approximations of Hyperbolic Equations, SIAM, 1982.
[34] T. Colonius, S. Lele, P. Moin, The free compressible vortex, J. Fluid Mech. 230 (1991) 45–73.
[35] R. Rogallo, Numerical Experiments in Homogeneous Turbulence, Tech. Rep. 81315, NASA Ames, 1981.
[36] J. Herring, J. McWilliams, Comparison of direct numerical simulation of two-dimensional turbulence with two point closure: the effects of intermittency, J. Fluid. Mech. 153 (1985) 229–242.